minerals

Article

Evidence for the Multi-Stage Petrogenetic History of the Oka Carbonatite Complex (Québec, Canada) as Recorded by Perovskite and Apatite

Wei Chen * and Antonio Simonetti

Department of Civil & Environmental Engineering & Earth Sciences, University of Notre Dame, 156 Fitzpatrick Hall, Notre Dame, IN 46556, USA; E-Mail: simonetti.3@nd.edu

* Author to whom correspondence should be addressed; E-Mail: wchen2@nd.edu;
   Tel.: +1-574-631-6710; Fax: +1-574-631-9236.

Abstract: The Oka complex is amongst the youngest carbonatite occurrences in North America and is associated with the Monteregian Igneous Province (MIP; Québec, Canada). The complex consists of both carbonatite and undersaturated silicate rocks (e.g., ijolite, alnöite), and their relative emplacement history is uncertain. The aim of this study is to decipher the petrogenetic history of Oka via the compositional, isotopic and geochronological investigation of accessory minerals, perovskite and apatite, using laser ablation inductively coupled plasma mass spectrometry (LA-ICP-MS). The new compositional data for individual perovskite and apatite grains from both carbonatite and associated alkaline silicate rocks are highly variable and indicative of open system behavior. *In situ* Sr and Nd isotopic compositions for these two minerals are also variable and support the involvement of several mantle sources. U-Pb ages for both perovskite and apatite define a bimodal distribution, and range between 113 and 135 Ma, which overlaps the range of ages reported previously for Oka and the entire MIP. The overall distribution of ages indicates that alnöite was intruded first, followed by okaite and carbonatite, whereas ijolite defines a bimodal emplacement history. The combined chemical, isotopic, and geochronological data is best explained by invoking the periodic generation of small volume, partial melts generated from heterogeneous mantle.

1. Introduction

Previous studies indicate that carbonatites worldwide range in age from the Archean to present day, with the frequency of occurrences increasing with decreasing age (*i.e.*, with those <200 Ma in age being the most abundant) [1]. The oldest known carbonatite on Earth is the Tupertalik complex (3.0 Ga; western Greenland) [2], and the youngest is the active natrocarbonatite volcano, Oldoinyo Lengai, Tanzania [3–7]. Among the 527 carbonatite occurrences identified and compiled by Woolley and Kjarsgaard [1], only 264 have been dated, with most ages determined by the K/Ar method and merely 6% investigated by U-Pb geochronology.

In North America, carbonatite and alkaline magmatism spans ~2.7 Ga [8,9], and Oka (Figure 1) is one of the youngest carbonatite complexes on the basis of available geochronological data for various minerals and/or rock types. Apatite fission track ages reported for Oka vary between 118 ± 4 and 133 ± 11 Ma [10], whereas Shafiquall *et al.* [11] document K-Ar ages that range between 107 and 119 Ma for the intrusive alnöites associated with the complex. Wen *et al.* [12] reported a Rb–Sr biotite-whole rock isochron age of 109 ± 2 Ma obtained by isotope dilution-thermal ionization mass spectrometry (ID-TIMS), whereas Cox and Wilton [13] obtained a U-Pb age of 131 ± 7 Ma for perovskite from carbonatite by laser ablation inductively coupled plasma mass spectrometry (LA-ICP-MS). Cox and Wilton [13] postulated that the variable ages obtained by either Rb-Sr or K-Ar methods for the Oka carbonatite complex most probably result from their lower closure temperatures (relative to the U-Pb isotope system).

In a recent study, Chen and Simonetti [14] conducted a detailed U-Pb geochronological investigation of apatite from carbonatite, okaite and melanite ijolite at Oka. The geochronological results define a bimodal age distribution with peaks at ~117 and ~125 Ma. Chen *et al.* [15] also reported *in-situ* U-Pb ages for niocalite [$Ca_{14}Nb_2(Si_2O_7)_2O_6F_2$] from carbonatite at Oka, a first documented radiometric study for this mineral. The results from the latter study corroborate the variable apatite U-Pb ages [14] since they also define a similar bimodal distribution with peak $^{206}Pb/^{238}U$ weighted mean ages at 133.2 ± 6.1 and 110.1 ± 5.0 Ma. Hence, these detailed investigations reporting *in-situ* U-Pb ages for apatite and niocalite from Oka offer a more comprehensive geochronological view of this complex, and clearly suggest a protracted magmatic history that spanned at least ~10 million years [14]. Of note, the protracted igneous activity outlined for Oka overlaps that for the entire range of ages reported for the remaining Monteregian Igneous Province (MIP)-related intrusions (118–135 Ma; Figure 1) [13–16].

Plutonic igneous bodies, such as the Oka carbonatite complex, may form as a result of sequential and episodic melting and crystallization events. These events may be traced by monitoring the chemical compositions of constituent minerals, whereas the timing of such events can be determined using precise geochronological methods (e.g., U-Pb dating). Rukhlov and Bell [9] emphasized the importance of incorporating data from several isotope systems (and mineral/rock phases) before concluding the definite emplacement ages for carbonatite complexes since these typically result from complicated petrogenetic histories. Moreover, accessory phases such as perovskite, apatite and niocalite are characterized by very high abundances (1000s of ppm) of incompatible elements such as Nd and Sr, which are important isotope tracers for delineating magmatic processes and potential mantle sources. Thus, the combined presence of several U- (and Pb-) bearing accessory minerals, such as apatite, niocalite and perovskite within carbonatite, together with the capability of obtaining precise

and accurate, spatially resolved chemical, isotopic, and geochronological data by laser ablation inductively (multi-collector) coupled plasma mass spectrometry (LA-(MC)-ICP-MS) analysis on individual (single) mineral grains renders the investigation of these accessory minerals a powerful tool in deciphering the formational history of carbonatite complexes.

Figure 1. (**A**) Regional map showing distribution of intrusions associated with the Monteregian Igneous Province (MIP) including the Oka carbonatite complex [14,17]. Intrusions identified on the map are: 1-Oka; 2-Royal; 3-Bruno; 4-St. Hilaire; 5-Rougemont; 6-Johnson; 7-Yamaska; 8-Shefford; 9-Brome. (**B**) Geological map of the Oka carbonatite complex [10,15]. The type localities of the Nb deposits within Oka are shown in the map: SLC: St. Lawrence Columbium, NIOCAN: name of mining company with mineral rights, and Bond Zone: NH = New Hampshire. Sample stop numbers correspond to those from the 1986 GAC-MAC-sponsored Oka field excursion [10].
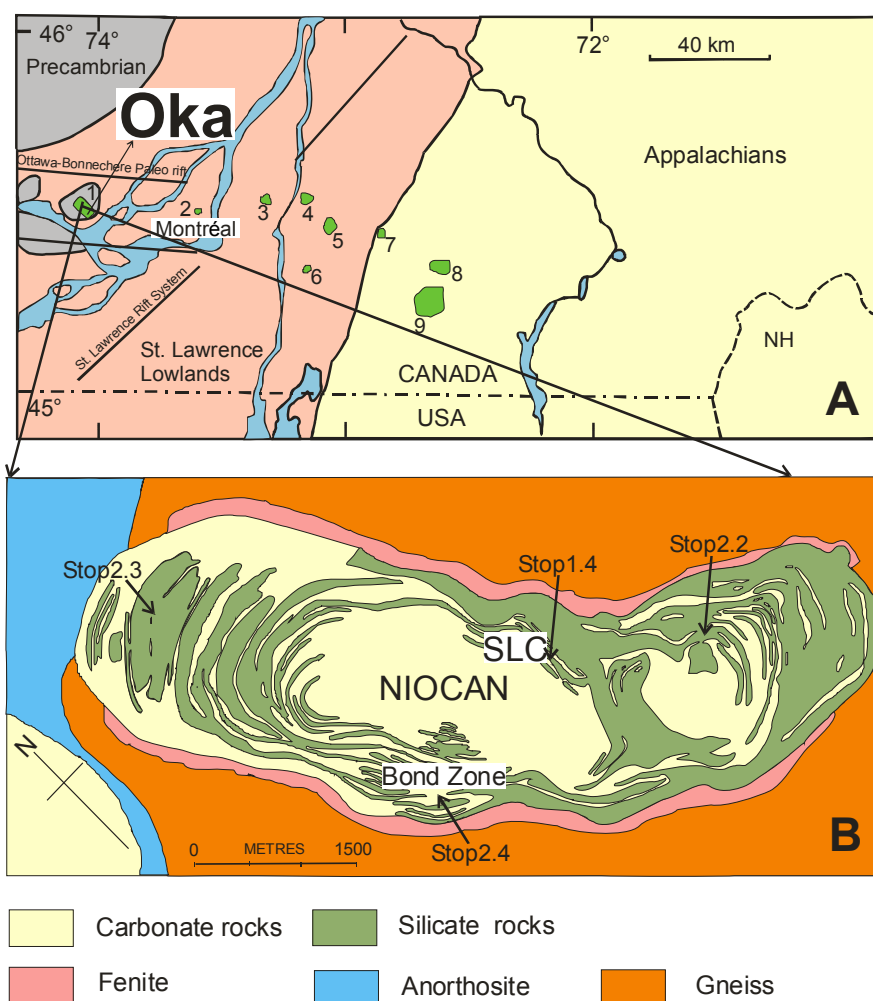
Perovskite, $CaTiO_3$, is a widespread accessory mineral in SiO_2-undersaturated and alkaline magmatic systems, and present within kimberlites, melilitites, foidites, olivinites, clinopyroxenites, ultramafic lamprophyres/carbonatites, and lamproites [18]. It typically forms throughout the melt crystallization sequence and serves as a major host for incompatible trace elements, such as the Rare Earth Elements (REEs) [18,19]. Furthermore, perovskite may preserve the original, magmatic radiogenic isotope

signatures that are frequently obscured in whole rock compositions because it is relatively resistant to post-solidification alteration [19]. Recently, perovskite has been the focus of petrogenetic studies involving alkaline magmatic systems because of its capacity to yield combined accurate geochronological, chemical and/or radiogenic isotope information [13,19–22]. Cox and Wilton [13] were the first to report an *in-situ* U-Pb geochronological investigation of perovskite from Oka by LA-ICP-MS; however, their study was not combined with any geochemical data, and hence does not provide any insights into possible melt differentiation processes. For example, the exact petrogenetic relationship between carbonatite and associated alkaline silicate rocks within an individual carbonatite complex remains somewhat elusive; models proposed include liquid immiscibility [23–26], protracted fractional crystallization of a carbonate-rich, Si-undersaturated parental melt [27–29], and small volume partial melts derived from metasomatized mantle [30–32].

This study focuses on a detailed chemical, isotopic and geochronological investigation of perovskite and apatite associated with alnöite and jacupirangite from the Oka carbonatite complex. We report new, *in-situ* major and trace element chemical compositions, Sr and Nd isotopic data, and U-Pb ages for perovskite and apatite. Hence, this study provides additional insights into the formational history of the Oka carbonatite complex, and compliments the earlier *in-situ* U-Pb investigations of apatite [14] and niocalite [15].

2. Background

2.1. Geological Setting and Description of Samples

The series of alkaline intrusions associated with the MIP define a linear E–W trend that roughly follows the Ottawa-Bonnechere Paleo-rift (Figure 1A) [33]. The Oka carbonatite complex, which is the most westerly intrusion, is located entirely within the Grenville Province and does not contain any quartz-bearing rocks (Figure 1B). Moving in a southeastward direction, the remaining complexes have intruded two different tectonic/structural terrains. Mounts Royal, St. Bruno, St. Hilaire, Rougemont, and Johnson are hosted by St. Lawrence Lowlands Cambrian-Ordovician dolostones, carbonates and shales; Mounts Brome and Shefford intrude the metasediments and metamorphic rocks of the Appalachians (Figure 1A) [33,34].

Gold *et al.* [10] provided a detailed description of the Oka carbonatite complex (Figure 1B). In summary, the complex consists of both carbonatite (Figure 2A) and Si-undersaturated rocks (*i.e.*, okaite, ijolite, alnöite, and jacupirangite; Figure 2B–E). The mineralogical descriptions of the samples investigated in this study are listed in Table 1, and all samples were retrieved from the Stop 2.3 locality with the exception of Oka88 (Stop 2.2; Figure 1B). Apatite is a common accessory mineral phase occurring in all rock types, and forms euhedral crystals, which vary between ~1 and ~100 μm in diameter (e.g., Figure 2A,E). Perovskite is present in most of the silicate rocks (*i.e.*, okaite and alnöite) and usually occurs as euhedral crystals characterized by pseudocubo-octahedral habit up to several cm in diameter (*i.e.*, Figure 2F,G). In two okaite samples (Oka229 and Oka137), perovskite exhibits zoning as evidenced in optical microscopy and back-scattered electron (BSE) imagery (e.g., Figure 2G,H). The zoning typically consists of a low average atomic number core and a high average atomic number rim of irregular thickness (Figure 2H).

Table 1. Summary of the mineralogy of the main rock types at Oka.

Rock Type	Carbonatite	Okaite (Melilitite)	Melanite ijolite	Ijolite	Alnoite	Jacupirangite
Calcite	60–95	5–10	2–10	0–5	0–5	-
Apatite	2–10	2–10	2–5	0–5	0–10	2–5
Magnetite	5–10	5–10	0–5	-	5–10	2–10
Perovskite	-	2–10	-	-	-	-
Melilite	-	60–90	-	-	-	-
Biotite	0–5	5–15	-	-	5–10	2–5
Melanite	-	-	20–40	-	-	-
Pyroxene	0–10	-	20–40	40–50	20–40	60–70
Nepheline	-	-	20–40	40–50		15–20
Olivine	-	-	-	-	10–25	-
Niocalite	0–10	-	-	-	-	-
Groundmass	-	-	-	-	30–60	-

Note: Mineral occurrences are reported in volume percent.

Figure 2. Petrographic images illustrating the mineralogy of the different rock types investigated here. (**A**) carbonatite- Oka51; (**B**) okaite- Oka138; (**C**) ijolite- Oka88; (**D**) alnöite- Oka87; (**E**) jacupirangite- Oka78; (**F**) perovskite in okaite Oka208; (**G**) zoned perovskite in okaite Oka229; (**H**) back-scattered electron image of the zoned perovskite in (**G**). Cal: calcite; Ap: apatite; Ox: oxide; Mll: melilite; Cpx: clinopyroxene; Nph: nephline; Prv: perovskite; Ol: olivine.
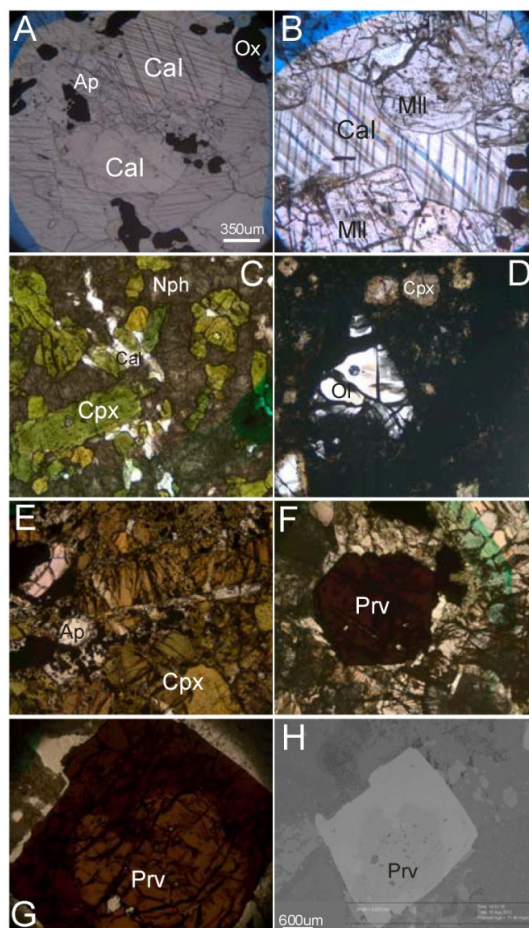
2.2. Analytical Methods

2.2.1. Chemical Analysis

Major and minor element concentrations for apatite and perovskite were determined using a Cameca SX50 electron microprobe (EMP; Cameca, Gennevilliers, France) at the University of Chicago. All thin sections were carbon-coated prior to analysis. The EMP analyses were conducted using a 15 kV accelerating potential and 30–35 nA incident current. The natural and synthetic mineral and glass standards employed for calibration purposes were: natural olivine (for Fe, Mn, Mg, and Si), natural albite (for Na), durango apatite (for P, F, and Ca), synthetic glass of anorthite composition (for Al), strontianite (for Sr), zircon (for Zr), synthetic NB metal (for Nb), synthetic TiO_2 (for Ti), synthetic REE_3 metal (for La, Ce, and Pr), synthetic REE_2 metal (for Nd and Sm), and synthetic TA metal (for Ta). Calculated apatite and perovskite formulae were normalized by stoichiometry.

In-situ trace element analyses of individual apatite and perovskite grains were obtained using a UP213 nm laser ablation system coupled to a Thermo-Finnigan Element2 sector field high-resolution ICP-MS (Thermo Fisher Scientific, Dreieich, Germany) housed within the Midwest Isotope and Trace Element Research Analytical Center (MITERAC) at the University of Notre Dame, and following the protocol by Chen and Simonetti [14] and Chen *et al.* [15]. The NIST SRM 610 international glass standard [35] was used for external calibration and ^{43}Ca ion signal intensities were employed as the internal standard with the CaO content (wt %) obtained by EMP analysis. The sample grains and standard were ablated using a 25 μm spot size, 4–5 Hz repetition rate, and corresponding energy density of ~10–12 J/cm^2. Data reduction, including concentration determinations, method detection limits and individual run uncertainties were obtained with the GLITTER laser ablation software [36].

2.2.2. U-Pb Age Dating by Laser Ablation (Multi-Collector) Inductively Coupled Plasma Mass Spectrometry

The instrumental configuration described above for the trace element determinations was also employed for the *in-situ* U-Pb isotope analyses. The analytical protocol adopted here is similar to that described in Simonetti and Neal [37] and Chen and Simonetti [14]. Data acquisition typically consisted of the first ~30 s for measurement of the background ion signals, followed by 30 s of ablation, and a minimum 15 s of washout time. Single mineral grains were ablated using a 40–55 μm spot size and corresponding fluence of ~3 J/cm^2 and repetition rate of 5 Hz. The following ion signals were acquired: ^{202}Hg, ^{204}(Pb + Hg), ^{206}Pb, ^{207}Pb, ^{208}Pb, ^{232}Th, ^{235}U, ^{238}U and $^{232}Th^{16}O$. ^{202}Hg was measured to monitor the ^{204}Hg interference on ^{204}Pb (using a $^{204}Hg/^{202}Hg$ value of 0.229883) [36]. In addition, U-Pb dates for some samples were determined using a NWR193 nm laser ablation system (ESI New Wave Research, Huntingdon, UK) coupled to a Nu Plasma II MC-ICP-MS instrument (Nu Instruments Ltd., Wrexham, UK) within the MITERAC facility at the University of Notre Dame. All masses of interest (^{202}Hg, ^{204}(Pb + Hg), ^{206}Pb, ^{207}Pb, and ^{208}Pb) can be simultaneously acquired using a combination of ion counters (Hg and Pb ion signals), and Faraday cups (^{232}Th and ^{238}U). Samples and standards were ablated employing a 55–75 μm spot size with corresponding fluence of ~10 J/cm^2 and 7 Hz repetition rate. Data acquisition consisted of the first ~40 s for background measurement, followed by ~60 s of ablation, and a minimum ~2 min of washout time.

Instrumental drift and laser induced elemental fractionation (LIEF) was monitored using a "standard-sample bracketing" technique. The Madagascar apatite [38] and Ice River perovskite [19] were adopted as the external standards for the U-Pb dating of apatite and perovskite, respectively. Each set of 10–12 unknown analyses was bracketed with five analyses of the pertinent standard both prior and after the unknown analyses. Instrumental drift and Pb-U laser induced fractionation were corrected based on the $^{206}Pb/^{238}U$ and $^{207}Pb/^{235}U$ ratios for the standards, *i.e.*, for the Madagascar apatite, the ratios are 0.0781 and 0.6123 [38], respectively; whereas for the Ice River perovskite, the adopted values are 0.0575 and 0.4270, respectively [19].

Apatite and perovskite are U-bearing accessory minerals that may contain a significant amount of common Pb. The ^{207}Pb-correction method was adopted here, which employs the Tera-Wasserburg Concordia plot and consequently is an approach that does not require knowledge of the accurate abundance of ^{204}Pb. This method was successfully employed in previous studies for a variety of common Pb-bearing accessory minerals, such as titanite [20,39–41], perovskite [13,19,20], apatite [14,41], and niocalite [15]. The ^{207}Pb-correction method does require knowledge, however, of the Pb isotope composition of the common Pb component. In this study, the latter is defined by the Pb isotope composition of the associated and ubiquitously present *U-free* calcite [14]. The $^{207}Pb/^{206}Pb$ ratio of 0.792 ± 0.06 [14,42] obtained for the latter is then applied to correct the measured $^{206}Pb/^{238}U$ ratios using well established common lead–radiogenic lead mixing equations [13,39].

Fragments of Emerald Lake and Durango apatites were used as secondary apatite standards and both are well characterized with ages of 90.5 ± 3.1 and 30.6 ± 2.3 Ma, respectively [43]. Repeated analyses of these two standards obtained during the course of this study yielded weighted mean $^{206}Pb/^{238}U$ ages of 92.6 ± 1.6 Ma ($n = 17$) and 31.9 ± 1.3 Ma ($n = 10$), respectively, and both are identical (given their associated uncertainties) to the ages reported by Chew *et al.* (Figure 3A,B) [41]. Of importance, U-Pb ages were obtained by both laser ablation multi-collector inductively coupled plasma mass spectrometry (LA-MC-ICP-MS) and LA-ICP-MS methods for the same apatite grains in one carbonatite sample (Oka147), and these yield identical dates (Figure 3C,D). These corroborative results in turn serve to further validate the analytical methods employed here.

Uncertainties associated with individual analyses, which include propagation of errors from individual measurements (based on counting statistics) and the relative standard deviation associated with repeated analyses of the Madagascar apatite and Ice River perovskite standards, were determined using the quadratic equation [38,44,45]. Isoplot v3.0 program was employed for constructing Tera-Wasserburg diagrams and determination of Concordia lower intercept ages, and $^{206}Pb/^{238}U$ weighted mean age calculations [46].

Figure 3. U-Pb isotopic ages for apatite secondary standards and sample. The U-Pb age of the secondary standard—Durango apatite is shown (**A**), and it is identical to the reported value (**B**) by Chew *et al.* [41]. Apatite from carbonatite Oka147 was dated by the laser ablation multi-collector inductively coupled plasma mass spectrometry (LA-MC-ICP-MS) (**C**) and LA-ICP-MS (**D**).
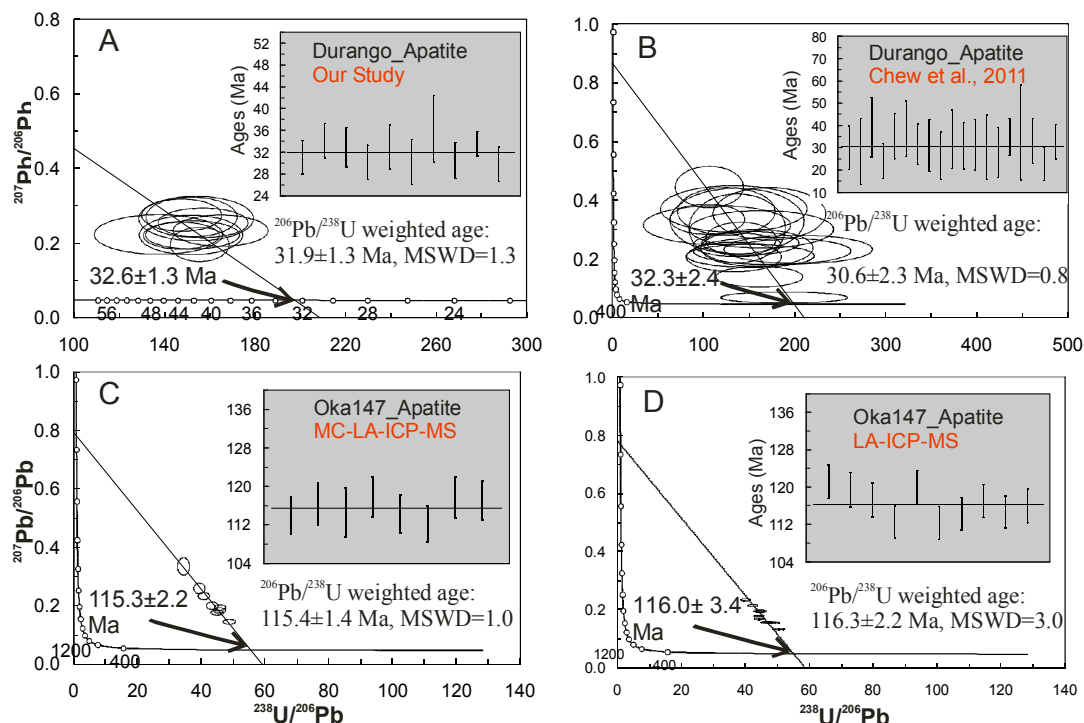
2.2.3. Sr and Nd Analysis by LA-(MC)-ICP-MS

In-situ Sr and Nd isotope ratios for perovskite and apatite were determined with a NWR193 laser ablation system coupled to a Nu Plasma II MC-ICP-MS instrument (Nu Instruments Ltd., Wrexham, UK). *In-situ* Sr isotope measurements involve correction of critical spectral interferences that include Kr, Rb, and doubly charged REEs [47,48]. These detailed corrections are adopted in this study and are identical to those reported in Chen *et al.* [15]. A modern-day coral (Indian Ocean) served as an external, in-house standard, which is well characterized for its $^{87}Sr/^{86}Sr$ isotopic composition by ID-TIMS [49]. The coral standard and perovskite grains were analyzed using a 75~100 μm spot size, 7 Hz repetition rate, and an energy density ~11 J/cm^2. The average $^{87}Sr/^{86}Sr$ ratio obtained for the coral standard is 0.70915 ± 0.00003 based on five measurements, and is indistinguishable (given uncertainties) compared to the corresponding TIMS value of 0.70910 ± 0.00002 [49].

In order to obtain accurate measurement of Nd isotope ratios, it is important to identify and correct isobaric interferences and monitor for instrumental mass discrimination. The isobaric interferences for *in-situ* Nd isotope determinations are principally related to Sm, Ce and Ba, and the correction of the ^{144}Sm ion signal on ^{144}Nd is critical. The $^{146}Nd/^{144}Nd$ ratio is traditionally selected to correct for instrumental mass discrimination with the $^{146}Nd/^{144}Nd_{ref} = 0.7219$ [50]. As described in Yang *et al.* [51], the mass bias for both Sm and Nd were set to be identical ($\beta Sm = \beta Nd$). The mass bias correction for Sm is based on the $^{149}Sm/^{144}Sm$, and consequently the ^{144}Nd ion signal can be calculated according to the following equation:

$$I_{144Nd} = I_{144(Nd+Sm)} - I_{149Sm} \times \left(\frac{^{144}Sm}{^{149}Sm} \right) \times \left(\frac{m_{149Sm}}{m_{144Sm}} \right)^{\beta Sm} \tag{1}$$

The Durango apatite was adopted as the external standard with the accepted $^{143}Nd/^{144}Nd = 0.512483$ [52]. The "standard-sample" bracketing method was used and both standard and samples were analyzed using a 75–100 μm spot size, 7 Hz repetition rate, and corresponding energy density of ~9 J/cm^2.

3. Results

3.1. Major and Trace Element Data

The major and trace element data for perovskite investigated in this study are listed in Tables 2 and 3. In total, >30 chemical analyses of perovskite from okaite (Oka229, Oka137, and Oka208), alnöite (Oka73), and jacupirangite (Oka70) were obtained. Based on their major element compositions, the data for perovskite plot into two groups, in particular relative to their Nb_2O_5 wt % abundances (Figure 4A). One group (Nb-E: Nb-enriched) contains high Nb_2O_5 contents (between 7.25 and 10.80 wt %), whereas the other (Nb-D: Nb-depleted) is characterized by lower Nb_2O_5 abundances (between 1.56 and 4.92 wt %). Table 2 shows that perovskite from both alnöite and jacupirangite belongs to the Nb-D group, whereas compositions for those from okaite are variable. Of importance, both Nb-E and Nb-D types of perovskite are present within individual samples (*i.e.*, Oka137 and Oka229) and even within singular zoned grains (e.g., Figure 5; in total two well-zoned grains have been identified). For example, the zoned perovskite grain shown in Figure 5 has a rim that consists of a Nb-E composition, whereas the central area is characterized by the Nb-D component. In general, Nb-E perovskite is characterized by high contents of Na, Al, Fe, Sr, Ta and REEs (Figure 4B,C; Tables 2 and 3). The composition for the Nb-E perovskite is not that of the ideal end-member, but can be described by involving components of lueshite ($NaNbO_3$), latrappite ($CaNb_{0.5}Fe_{0.5}O_3$), and (LREE)FeO_3 (light REEs), which form by elemental substitutions into the structure at both Ca and Ti sites [53,54]. Molar percentages of different perovskite endmembers are also listed in Table 2. The most significant substituents in the Ca site are REEs and Na (Figure 4B), which comprise up to 8.70 mol % of the (LREE)FeO_3 component in some Nb-E perovskite (Table 2). Another example is the coupled substitution between Ti and Nb + Fe^{3+} or Nb + Al, which accounts for up to 10.96 mol % of $CaNb_{0.5}Fe_{0.5}O_3$ (latrappite) or $CaNb_{0.5}Al_{0.5}O_3$ (Figure 4C; Table 2).

The total REE budget for perovskite is dominated by the light REEs (LREEs; *i.e.*, La, Ce, Pr, Nd) abundances with (La/Yb)$_{CN}$ ratios that vary between 364 and 1652 (Table 3), and as illustrated by the pronounced, negatively-sloped chondrite-normalized REE patterns (Figure 6). Pb and Th abundances for perovskite both define negative correlations with Ca contents and suggest their substitution within the same Ca site (Figure 7A,B); in contrast, U abundances do not show any covariance with Ca contents (not shown). Of note, some elements are reported for both EMP and LA-ICP-MS analysis (e.g., LREEs). For example, the relative difference in the measured abundances of Pr obtained by these two methods is ~10%.

Table 2. Major element compositions of perovskite from the Oka complex.

Sample	Oka70 (Jacupirangite)				Oka73 (Alnoite)				
	PV1	PV2	PV3	PV4	PV3	PV4	PV7	PV8	PV9
Nb_2O_5	2.15	2.12	2.26	1.67	2.90	1.66	1.56	3.99	1.26
Ta_2O_5	0.01	0.00	0.18	0.05	0.10	0.43	0.15	0.14	0.07
SiO_2	0.01	0.00	0.01	0.01	0.00	0.00	0.00	0.00	0.00
TiO_2	52.45	52.72	52.27	52.09	49.75	48.81	53.07	45.98	53.82
ZrO_2	0.07	0.08	0.06	0.05	0.25	0.06	0.02	0.28	0.14
Al_2O_3	0.40	0.40	0.43	0.48	0.48	0.54	0.37	0.52	0.21
Fe_2O_3	2.66	2.48	2.72	2.68	3.34	4.03	2.16	4.94	1.82
La_2O_3	0.85	0.90	0.93	0.88	1.72	2.08	1.33	2.32	0.93
Ce_2O_3	1.49	1.46	2.04	1.82	3.19	4.48	2.70	5.24	1.52
Pr_2O_3	0.12	0.13	0.22	0.23	0.39	0.50	0.22	0.54	0.14
Nd_2O_3	0.42	0.50	0.65	0.61	0.98	1.72	0.93	1.88	0.45
Sm_2O_3	0.09	0.04	0.08	0.06	0.16	0.09	0.00	0.19	0.05
CaO	37.98	38.22	37.58	38.01	36.36	34.58	36.94	33.13	38.75
SrO	0.52	0.54	0.48	0.49	0.38	0.25	0.43	0.39	0.40
Na_2O	0.31	0.31	0.35	0.28	0.38	0.38	0.38	0.70	0.23
Total	99.01	99.43	99.74	98.87	99.74	98.83	99.84	99.29	99.43
Structural formulae									
Nb^{5+}	0.023	0.022	0.024	0.018	0.031	0.018	0.017	0.042	0.013
Ta^{5+}	0.000	0.000	0.001	0.000	0.001	0.003	0.001	0.001	0.000
Si^{4+}	0.000	0.000	0.000	0.000	0.000	0.000	0.000	0.000	0.000
Ti^{4+}	0.925	0.929	0.922	0.918	0.877	0.861	0.936	0.811	0.949
Zr^{4+}	0.000	0.000	0.000	0.000	0.001	0.000	0.000	0.002	0.001
Al^{3+}	0.011	0.011	0.012	0.013	0.013	0.015	0.010	0.014	0.006
Fe^{3+}	0.047	0.044	0.048	0.047	0.059	0.071	0.038	0.087	0.032
La^{3+}	0.007	0.008	0.008	0.008	0.015	0.018	0.011	0.020	0.008
Ce^{3+}	0.013	0.013	0.018	0.016	0.027	0.038	0.023	0.045	0.013
Pr^{3+}	0.001	0.001	0.002	0.002	0.003	0.004	0.002	0.005	0.001
Nd^{3+}	0.004	0.004	0.005	0.005	0.008	0.014	0.008	0.016	0.004
Sm^{3+}	0.001	0.000	0.001	0.000	0.001	0.001	0.000	0.002	0.000
Ca^{2+}	0.954	0.960	0.944	0.954	0.913	0.868	0.927	0.832	0.973
Sr^{2+}	0.007	0.007	0.007	0.007	0.005	0.003	0.006	0.005	0.005
Na^+	0.014	0.014	0.016	0.013	0.017	0.017	0.017	0.032	0.011
mol % of the endmembers									
$CaTiO_3$	93.68	93.63	93.00	93.25	89.46	89.62	93.79	85.43	94.84
$CaNb_{0.5}(Fe,Al)_{0.5}O_3$	2.89	3.00	2.18	3.61	3.51	0.75	0.00	2.06	2.33
$NaNbO_3$	0.86	0.76	1.44	0.01	1.44	1.73	1.73	3.36	0.21
$(LREE)FeO_3$	2.57	2.61	3.37	3.12	5.59	7.89	4.48	9.15	2.62

Table 2. *Cont.*

Sample	PV1	PV1_2	PV2_1	PV2_2	PV2_3	PV2_4	PV2_5	PV2_6	PV2_7	PV2_8
					Oka229 (Okaite)					
			Rim	Core	Core	Core	Rim	Rim		
Nb_2O_5	3.71	3.60	10.43	4.92	4.76	4.74	9.77	10.14	7.25	7.25
Ta_2O_5	0.31	0.17	0.80	0.17	0.20	0.21	0.92	0.90	0.38	0.43
SiO_2	0.00	0.00	0.17	0.00	0.02	0.05	0.12	0.04	0.02	0.05
TiO_2	47.01	48.15	38.86	46.26	46.18	46.72	39.62	39.44	42.95	43.26
ZrO_2	1.35	0.98	0.35	0.90	0.81	0.83	0.34	0.21	0.34	0.39
Al_2O_3	0.74	0.75	0.87	0.73	0.70	0.74	0.85	0.74	0.86	0.77
Fe_2O_3	4.30	4.04	6.18	4.33	4.09	4.35	6.04	6.02	5.26	5.51
La_2O_3	1.02	1.03	2.33	1.23	1.18	1.07	2.35	2.41	1.94	1.67
Ce_2O_3	2.71	2.65	4.64	2.72	2.55	2.65	4.75	4.94	4.27	4.17
Pr_2O_3	0.29	0.27	0.46	0.34	0.22	0.24	0.44	0.45	0.46	0.46
Nd_2O_3	1.11	1.12	1.38	0.97	0.99	0.95	1.44	1.46	1.41	1.42
Sm_2O_3	0.15	0.16	0.08	0.15	0.07	0.04	0.16	0.11	0.14	0.14
CaO	37.15	37.24	31.39	37.02	37.15	37.20	31.45	31.07	33.48	33.76
SrO	0.22	0.22	0.52	0.22	0.20	0.21	0.52	0.57	0.44	0.40
Na_2O	0.08	0.09	1.15	0.11	0.12	0.12	1.18	1.34	0.72	0.65
Total	99.32	99.71	98.44	99.24	98.45	99.29	98.81	98.68	98.93	99.29
					Structural formulae					
Nb^{5+}	0.039	0.038	0.110	0.052	0.050	0.050	0.104	0.107	0.077	0.077
Ta^{5+}	0.002	0.001	0.005	0.001	0.001	0.001	0.006	0.006	0.002	0.003
Si^{4+}	0.000	0.000	0.004	0.000	0.000	0.001	0.003	0.001	0.000	0.001
Ti^{4+}	0.829	0.849	0.685	0.816	0.814	0.824	0.699	0.695	0.757	0.763
Zr^{4+}	0.008	0.006	0.002	0.005	0.005	0.005	0.002	0.001	0.002	0.002
Al^{3+}	0.020	0.021	0.024	0.020	0.019	0.020	0.023	0.020	0.024	0.021
Fe^{3+}	0.076	0.071	0.109	0.076	0.072	0.077	0.107	0.106	0.093	0.097
La^{3+}	0.009	0.009	0.020	0.011	0.010	0.009	0.020	0.021	0.017	0.014
Ce^{3+}	0.023	0.023	0.040	0.023	0.022	0.023	0.041	0.042	0.037	0.036
Pr^{3+}	0.002	0.002	0.004	0.003	0.002	0.002	0.004	0.004	0.004	0.004
Nd^{3+}	0.009	0.009	0.012	0.008	0.008	0.008	0.012	0.012	0.012	0.012
Sm^{3+}	0.001	0.001	0.001	0.001	0.001	0.000	0.001	0.001	0.001	0.001
Ca^{2+}	0.933	0.935	0.788	0.930	0.933	0.934	0.790	0.780	0.841	0.848
Sr^{2+}	0.003	0.003	0.007	0.003	0.003	0.003	0.007	0.008	0.006	0.005
Na^+	0.004	0.004	0.052	0.005	0.006	0.005	0.054	0.061	0.033	0.030
					mol % of the endmembers					
$CaTiO_3$	86.76	87.41	75.41	84.58	85.14	85.08	76.31	75.71	80.48	81.12
$CaNb_{0.5}(Fe,Al)_{0.5}O_3$	8.57	8.03	10.59	10.96	10.74	10.58	9.36	8.99	8.60	8.64
$NaNbO_3$	0.00	0.00	5.70	0.00	0.00	0.00	5.85	6.61	3.47	3.14
$(LREE)FeO_3$	4.67	4.56	8.30	4.46	4.13	4.34	8.48	8.70	7.45	7.11

Table 2. *Cont.*

Sample	Oka137 (Okaite)					Oka209 (Okaite)				
	PV1_1	PV1_2	PV3	PV4	PV5	PV2	PV3_1	PV3_2	PV4	PV5
	Core	Rim								
Nb_2O_5	3.53	10.80	10.62	9.61	9.93	1.63	1.78	1.60	1.73	1.66
Ta_2O_5	0.28	1.02	0.87	0.76	0.67	0.06	0.14	0.02	0.04	0.04
SiO_2	0.01	0.00	0.00	0.01	0.00	0.00	0.01	0.00	0.00	0.00
TiO_2	47.82	39.23	39.48	40.01	40.12	52.46	52.53	52.94	52.39	51.84
ZrO_2	0.99	0.19	0.40	0.40	0.42	0.07	0.06	0.03	0.08	0.07
Al_2O_3	0.75	0.75	0.74	0.84	0.73	0.42	0.44	0.41	0.46	0.48
Fe_2O_3	4.09	6.11	5.65	5.80	5.90	2.40	2.54	2.36	2.37	2.69
La_2O_3	0.92	2.46	2.03	1.93	2.14	1.18	1.15	1.16	1.20	0.91
Ce_2O_3	2.66	4.74	4.21	4.23	4.44	2.11	2.10	2.06	2.10	1.95
Pr_2O_3	0.32	0.43	0.45	0.40	0.43	0.17	0.20	0.12	0.15	0.21
Nd_2O_3	1.05	1.42	1.30	1.32	1.34	0.72	0.64	0.65	0.67	0.56
Sm_2O_3	0.08	0.09	0.11	0.02	0.08	0.07	0.06	0.09	0.01	0.03
CaO	37.12	31.24	31.62	32.82	32.35	37.79	37.75	38.05	37.62	37.86
SrO	0.20	0.56	0.51	0.48	0.51	0.44	0.52	0.47	0.47	0.47
Na_2O	0.09	1.38	1.31	1.00	1.19	0.29	0.30	0.28	0.29	0.29
Total	99.14	99.24	98.23	98.52	99.12	99.35	99.71	99.79	99.15	98.55
Structural formulae										
Nb^{5+}	0.037	0.114	0.113	0.102	0.105	0.017	0.019	0.017	0.018	0.018
Ta^{5+}	0.002	0.006	0.006	0.005	0.004	0.000	0.001	0.000	0.000	0.000
Si^{4+}	0.000	0.000	0.000	0.000	0.000	0.000	0.000	0.000	0.000	0.000
Ti^{4+}	0.843	0.692	0.696	0.705	0.707	0.925	0.926	0.933	0.924	0.914
Zr^{4+}	0.006	0.001	0.002	0.002	0.002	0.000	0.000	0.000	0.000	0.000
Al^{3+}	0.021	0.021	0.020	0.023	0.020	0.012	0.012	0.011	0.013	0.013
Fe^{3+}	0.072	0.108	0.100	0.102	0.104	0.042	0.045	0.042	0.042	0.047
La^{3+}	0.008	0.021	0.018	0.017	0.018	0.010	0.010	0.010	0.010	0.008
Ce^{3+}	0.023	0.041	0.036	0.036	0.038	0.018	0.018	0.018	0.018	0.017
Pr^{3+}	0.003	0.004	0.004	0.003	0.004	0.001	0.002	0.001	0.001	0.002
Nd^{3+}	0.009	0.012	0.011	0.011	0.011	0.006	0.005	0.005	0.006	0.005
Sm^{3+}	0.001	0.001	0.001	0.000	0.001	0.001	0.000	0.001	0.000	0.000
Ca^{2+}	0.932	0.784	0.794	0.824	0.812	0.949	0.948	0.955	0.945	0.951
Sr^{2+}	0.003	0.008	0.007	0.007	0.007	0.006	0.007	0.006	0.006	0.006
Na^+	0.004	0.063	0.060	0.046	0.054	0.013	0.014	0.013	0.013	0.013
mol % of the endmembers										
$CaTiO_3$	87.50	74.85	75.69	75.54	75.59	93.37	93.37	93.68	93.50	93.17
$CaNb_{0.5}(Fe,Al)_{0.5}O_3$	8.07	9.90	10.35	12.40	10.93	2.36	2.13	2.19	2.07	3.63
$NaNbO_3$	0.00	6.81	6.47	4.87	5.80	0.60	0.92	0.62	0.85	0.00
$(LREE)FeO_3$	4.42	8.44	7.50	7.19	7.68	3.67	3.58	3.50	3.59	3.19

Table 2. *Cont.*

Sample	Oka208 (Okaite)					
	PV1	**PV2**	**PV3**	**PV5**	**PV6**	**PV7**
Nb_2O_5	2.55	3.13	2.86	3.30	3.14	2.70
Ta_2O_5	0.18	0.16	0.13	0.20	0.09	0.20
SiO_2	0.02	0.01	0.00	0.00	0.00	0.01
TiO_2	49.63	48.17	49.81	49.52	49.99	49.88
ZrO_2	0.04	0.07	0.06	0.07	0.05	0.07
Al_2O_3	0.55	0.53	0.61	0.51	0.52	0.58
Fe_2O_3	3.10	3.05	3.18	3.23	3.02	3.04
La_2O_3	1.27	1.32	1.37	1.35	1.38	1.35
Ce_2O_3	2.83	2.97	2.92	2.99	2.86	2.89
Pr_2O_3	0.27	0.33	0.35	0.28	0.26	0.30
Nd_2O_3	0.96	1.04	0.95	1.02	1.00	0.95
Sm_2O_3	0.08	0.09	0.17	0.04	0.12	0.10
CaO	35.60	36.32	36.45	35.75	36.01	36.21
SrO	0.47	0.49	0.52	0.51	0.53	0.51
Na_2O	0.54	0.42	0.39	0.45	0.45	0.39
Total	97.50	97.53	99.15	98.61	98.84	98.61
Structural formulae						
Nb^{5+}	0.027	0.033	0.030	0.035	0.033	0.029
Ta^{5+}	0.001	0.001	0.001	0.001	0.001	0.001
Si^{4+}	0.000	0.000	0.000	0.000	0.000	0.000
Ti^{4+}	0.875	0.849	0.878	0.873	0.881	0.879
Zr^{4+}	0.000	0.000	0.000	0.000	0.000	0.000
Al^{3+}	0.015	0.015	0.017	0.014	0.014	0.016
Fe^{3+}	0.055	0.054	0.056	0.057	0.053	0.054
La^{3+}	0.011	0.011	0.012	0.012	0.012	0.012
Ce^{3+}	0.024	0.026	0.025	0.026	0.025	0.025
Pr^{3+}	0.002	0.003	0.003	0.002	0.002	0.003
Nd^{3+}	0.008	0.009	0.008	0.009	0.008	0.008
Sm^{3+}	0.001	0.001	0.001	0.000	0.001	0.001
Ca^{2+}	0.894	0.912	0.915	0.898	0.904	0.909
Sr^{2+}	0.006	0.007	0.007	0.007	0.007	0.007
Na^+	0.025	0.019	0.018	0.020	0.020	0.018
mol % of the endmembers						
$CaTiO_3$	91.29	89.23	89.90	90.38	90.63	90.51
$CaNb_{0.5}(Fe,Al)_{0.5}O_3$	1.89	6.52	3.77	2.49	2.33	2.99
$NaNbO_3$	1.99	0.32	1.30	2.11	2.10	1.58
$(LREE)FeO_3$	4.83	3.93	5.03	5.02	4.93	4.92

Notes: Major element compositions are presented in wt %. Structural formulae are calculated based on 3 atoms of oxygen. The mol % of the endmembers are calculated following the sequence: (1) Ti^{4+} is assigned for $CaTiO_3$; (2) latrappite is calculated based on the availability of Ca^{2+}, Nb^{5+}, Fe^{3+} and Al^{3+}; (3) depends on the available Na^+ and Nb^{5+}, mol % of $NaNbO_3$ is calculated; and (4) the rest of the Fe^{3+} is combined with the $LREE^{3+}$ to $(LREE)FeO_3$.

Table 3. Trace element abundances of perovskite.

Sample	Oka70 (Jacupirangite)				Oka73 (Alnoite)				
	PV1	**PV2**	**PV3**	**PV4**	**PV3**	**PV4**	**PV7**	**PV8**	**PV9**
Mn	490	475	493	435	452	440	327	637	506
Mn	490	475	493	435	452	440	327	637	506
Ga	12	11	13	11	18	20	14	30	24
Sr	3,599	3,412	3,616	3,444	2,951	1,862	3,073	2,828	3,709
Y	232	240	307	205	156	407	144	268	347
Zr	288	243	247	214	433	2,488	68	1,494	600
Ba	55	50	64	51	91	104	70	143	111
La	6,020	8,086	8,177	6,054	10,489	14,881	8,296	14,658	10,781
Ce	10,488	13,001	1,7787	12,401	19,381	31,900	16,769	32,891	17,526
Pr	914	1,287	1,641	1,260	1,858	3,382	1,801	3,341	1,521
Nd	2,891	4,298	5,504	4,057	5,784	11,918	5,641	11,492	5,114
Sm	387	513	673	468	571	1,323	559	1,187	628
Eu	116	133	173	129	138	284	136	244	183
Gd	198	250	321	217	222	545	215	457	310
Tb	26	29	39	26	25	59	24	48	37
Dy	98	104	135	91	75	190	71	135	138
Ho	14	15	18	12	10	25	9	17	20
Er	28	30	40	26	24	58	22	42	42
Tm	2.4	2.4	3.0	2.0	1.5	4.8	1.3	2.7	3.9
Yb	11.2	11.2	14.9	9.8	8.7	24.7	6.3	13.9	18.5
Lu	1.1	0.9	1.3	0.8	0.8	2.6	0.4	1.5	1.7
Hf	7.5	6.9	6.4	5.6	10.0	48.9	1.8	44.1	15.8
Ta	243	395	376	353	460	5,412	622	427	177
Pb	5	8	10	9	21	36	24	45	14
Th	219	478	688	426	761	1403	1,282	2,417	229
U	144	110	111	112	124	124	113	101	206
(La/Yb)N	364	490	372	421	819	409	895	715	396

Sample	Oka229 (Okaite)									
	PV1	**PV1_2**	**PV2_1**	**PV2_2**	**PV2_3**	**PV2_4**	**PV2_5**	**PV2_6**	**PV2_7**	**PV2_8**
			Rim	Core	Core	Core	Rim	Rim		
Mn	306	536	802	338	525	332	853	750	681	791
Ga	13	15	22	16	16	13	23	22	19	21
Sr	1,689	1,962	3,465	1,623	1,710	1,770	3,568	3,668	2,813	3,072
Y	312	255	145	299	293	262	147	115	214	199
Zr	5,862	3,661	1,347	4,039	3,975	3,967	1,350	622	1,660	1,616
Ba	71	83	114	83	81	70	117	116	100	111
La	7,549	7,565	15,129	10,849	9,278	7,877	15,016	13,962	13,081	11,088
Ce	19,887	19,407	29,922	23,870	19,961	19,381	30,154	28,404	28,579	27,510
Pr	2,299	2,455	2,946	2,524	2,257	2,097	3,046	2,862	2,944	2,951
Nd	7,905	7,954	8,672	8,267	7,527	6,781	8,893	8,182	9,185	9,116
Sm	922	850	769	915	862	751	790	684	914	881
Eu	229	209	165	231	224	200	173	147	209	200
Gd	381	336	274	375	368	318	286	236	341	330

Table 3. *Cont.*

Sample	Oka229 (Okaite)

Sample	PV1	PV1_2	PV2_1	PV2_2	PV2_3	PV2_4	PV2_5	PV2_6	PV2_7	PV2_8
			Rim	Core	Core	Core	Rim	Rim		
Tb	45	39	30	43	42	37	31	25	38	36
Dy	151	127	82	142	143	123	83	65	111	106
Ho	20	16	10	19	18	16	11	8	14	13
Er	42	37	27	42	41	36	27	23	35	33
Tm	3.1	2.8	1.7	3.2	3.0	2.8	1.4	1.1	2.3	2.2
Yb	17.6	14.3	7.4	17.1	16.8	15.0	8.4	5.7	13.1	10.3
Lu	1.4	1.1	0.7	1.3	1.5	1.2	0.6	0.4	1.1	0.9
Hf	50.4	20.1	29.9	21.1	25.3	21.8	27.9	16.5	19.7	23.0
Ta	1,412	1,264	3,945	1,055	1,165	1,141	3,833	3,485	1,934	2,412
Pb	5	9	37	6	5	5	43	29	31	35
Th	194	238	1,746	255	97	95	2,224	1,162	1,558	1,889
U	191	186	71	209	188	210	70	58	183	152
$(La/Yb)_N$	291	360	1,391	431	375	356	1,219	1,652	680	728

Sample	\multicolumn{5}{c}{Oka137 (Okaite)}	\multicolumn{5}{c}{Oka209 (Okaite)}

Sample	PV1_1	PV1_2	PV3	PV4	PV5	PV2	PV3_1	PV3_2	PV4	PV5
	core	rim								
Mn	289	719	865	807	683	348	353	416	319	374
Ga	16	23	25	23	21	8	9	9	13	8
Sr	1,656	3,473	3,711	3,611	3,492	4,025	3,155	3,352	3,047	3,095
Y	367	182	165	189	144	190	214	258	204	185
Zr	5,427	1,508	1,481	1,817	1,535	240	279	276	250	213
Ba	73	106	119	111	87	49	49	54	84	52
La	7,515	16,177	15,177	13,939	8,859	6,870	8,551	8,771	8,335	7,076
Ce	21,468	31,025	31,244	30,380	18,276	12,187	15,534	15,508	14,481	15,036
Pr	2,299	2,926	3,093	2,974	1,735	944	815	794	829	893
Nd	8,239	9,030	9,391	9,275	5,398	4,066	4,643	4,747	4,503	4,210
Sm	969	817	849	847	562	467	532	551	511	492
Eu	232	171	178	177	135	119	137	147	129	133
Gd	459	337	321	329	211	227	292	301	250	245
Tb	53	38	35	36	24	26	33	35	29	29
Dy	170	97	92	98	72	91	114	121	92	94
Ho	23	12	11	13	9	12	15	16	12	12
Er	53	35	32	33	23	28	36	36	30	27
Tm	3.6	1.8	1.7	1.9	1.6	2.0	2.1	2.8	1.9	1.8
Yb	20.5	9.4	7.9	9.6	8.1	9.0	10.7	12.0	8.8	9.4
Lu	1.7	0.8	0.7	0.9	0.7	0.7	0.9	1.0	0.9	0.7
Hf	46.9	35.0	32.3	41.3	15.8	7.1	9.5	7.6	7.5	6.3
Ta	1,527	4,131	4,305	3,761	1,249	353	409	438	394	341
Pb	5	40	46	40	19	8	9	9	9	9
Th	192	2,504	2,630	2,327	845	409	494	517	487	413
U	164	79	63	86	103	100	102	127	113	110
$(La/Yb)_N$	249	1,165	1,313	991	745	516	545	496	641	510

<div align="center">Table 3. <i>Cont.</i></div>

Sample	Oka208 (Okaite)					
	PV1	**PV2**	**PV3**	**PV5**	**PV6**	**PV7**
Mn	346	318	342	358	352	415
Ga	13	17	14	15	13	17
Sr	3,219	3,592	3,532	3,338	3,548	3,488
Y	201	169	186	171	162	174
Zr	236	222	242	233	215	279
Ba	82	94	78	81	77	97
La	8,624	7,369	9,318	8,351	8,341	10,879
Ce	19,084	16,432	19,665	18,405	17,216	23,169
Pr	1,872	1,734	1,899	1,890	1,852	2,394
Nd	6,320	5,601	6,255	6,102	5,887	7,449
Sm	662	590	630	619	581	705
Eu	154	139	150	151	143	167
Gd	273	230	257	245	231	270
Tb	30	26	29	27	26	31
Dy	94	79	90	84	77	88
Ho	13	10	12	11	10	11
Er	28	23	27	24	24	26
Tm	2.0	1.4	1.8	1.6	1.4	1.7
Yb	9.4	7.1	8.4	7.8	7.3	8.9
Lu	0.8	0.6	0.7	0.6	0.6	0.6
Hf	5.5	5.5	5.6	5.4	4.8	6.1
Ta	776	724	801	866	722	864
Pb	17	15	16	22	17	19
Th	1,179	1,002	1,125	1,337	1,016	1,149
U	79	76	81	91	88	97
(La/Yb)N	624	708	754	724	778	833

<div align="center">Note: Trace element concentrations are listed in ppm.</div>

Figure 4. Compositional variation diagrams for perovskite from Oka. (**A**) TiO_2 *vs.* Nb_2O_5, with Nb-E and Nb-D groups identified; (**B**) $(Na^+ + LREE^{3+})$ *vs.* Ca^{2+}; (**C**) $(Al^{3+} + Fe^{3+} + Nb^{5+})$ *vs.* Ti^{4+}.
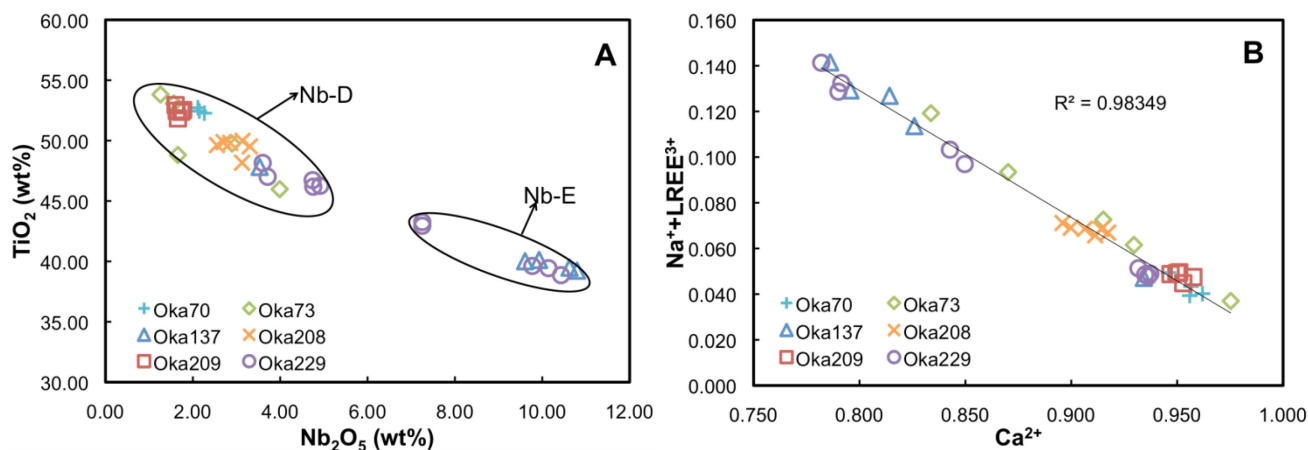
Figure 4. *Cont.*
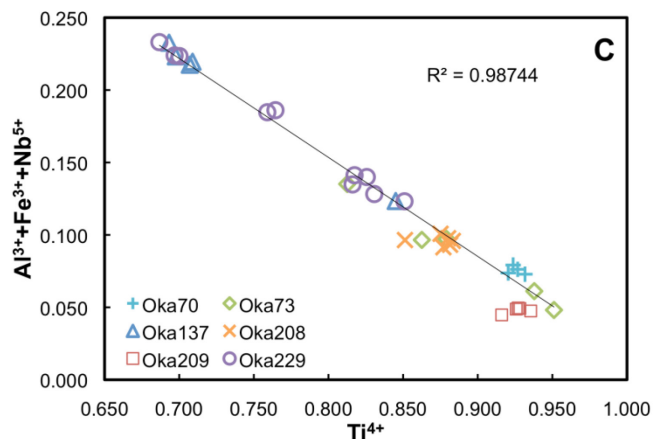
Figure 5. Petrographic image showing the zonation of perovskite. (**A**) U (ppm) concentrations obtained by LA-ICPMS with a 25 μm spot size; (**B**) Nb_2O_5 (wt %) abundances analyzed by EMP with a 5 µm beam; and (**C**) $^{206}Pb/^{238}U$ weighted mean ages (determined by LA-MC-ICPMS using a spot size of 75 μm) across a zoned perovskite grain from sample Oka229 (okaite).
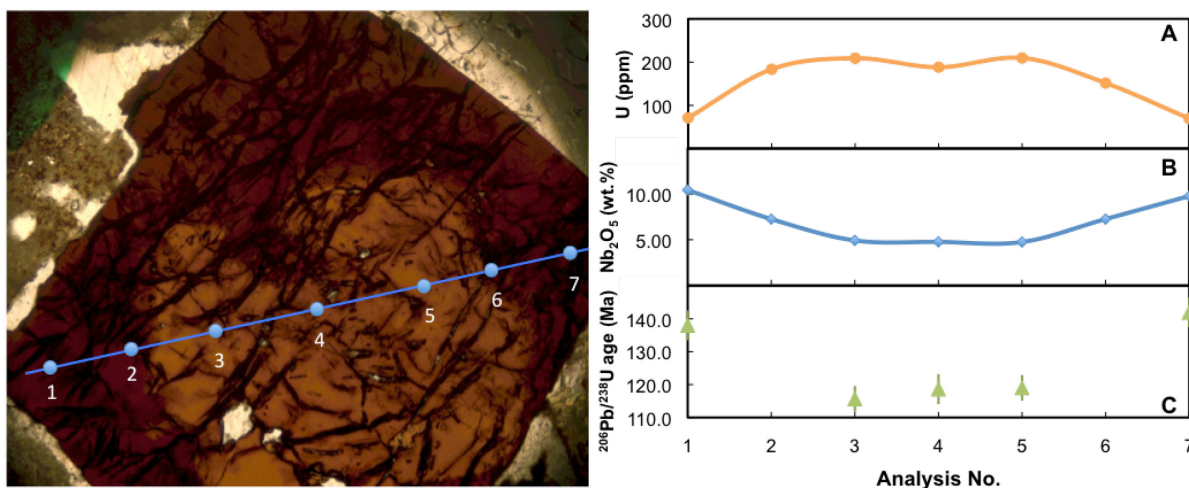
Figure 6. Chondrite normalized Rare Earth Element (REE) patterns for perovskite from alkaline silicate samples at Oka. Chondrite values are from McDonough and Sun [55].
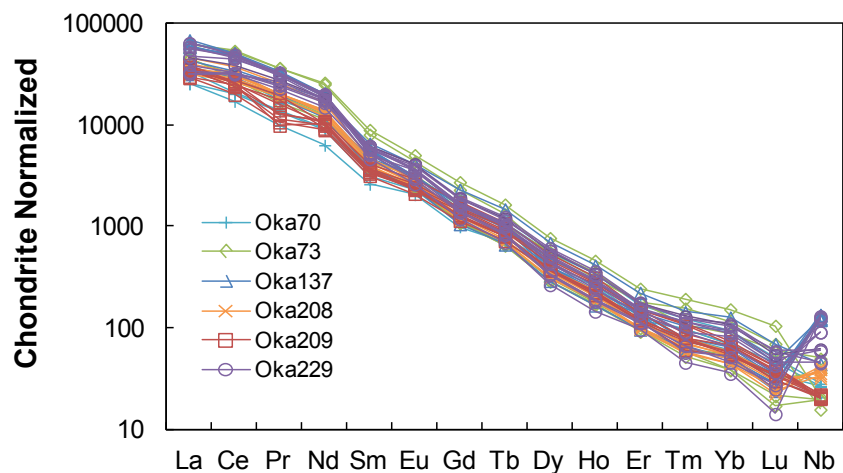
Figure 7. Plots exhibiting the correlations between Pb (**A**) and Th (**B**) abundances *vs.* Ca^{2+} (a.p.f.u.) for perovskite from Oka.
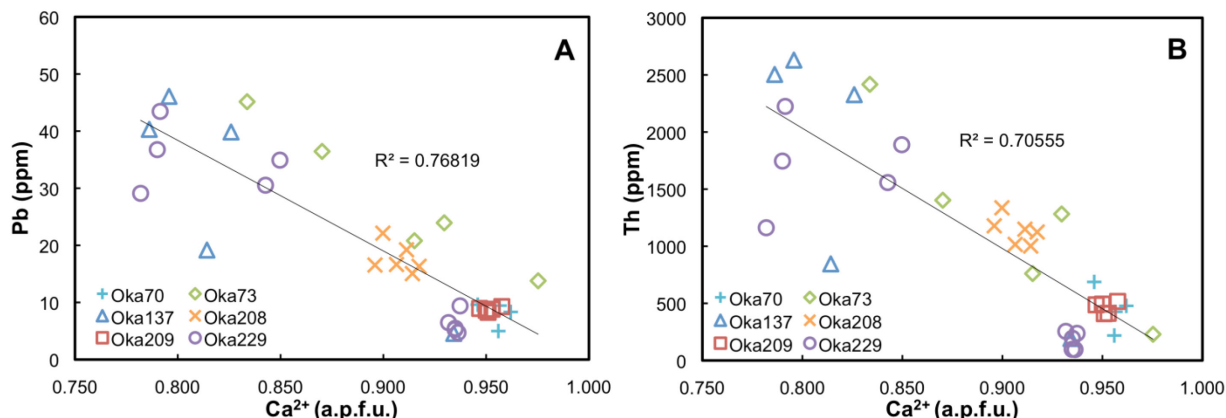
Newly obtained chemical compositions for apatite from alnöite, ijolite and jacupirangite are listed in Tables 4 and 5. Figure 8 plots the major element and LREE compositions for apatite from all rock types investigated here, along with those from carbonatite and okaite (Chen and Simonetti [14]). The compositions of fluorapatite from alnöite and jacupirangite are chemically distinct relative to the remaining rock types at Oka (Figure 8), *i.e.*, they contain a higher Ca content for a given P abundance (Figure 8A). As explained by Chen and Simonetti [14], REE abundances for apatite exhibit a positive correlation with Si contents due to their co-substitution within Ca and P structural sites. Once again, the same substitution scheme is evidenced here for all the apatites with the exception of those from alnöite and jacupirangite (Figure 8B). Chondrite normalized REE patterns for apatite investigated here are also negatively-sloped (Figure 9), but are more variable compared to those for perovskite (Figure 6). Of note, the chondrite normalized REE patterns for apatite from alnöite and jacupirangite exhibit less negative slopes among all rock types, with lower LREE abundances and comparable heavy REE (HREE) contents (Figure 9). $(La/Yb)_N$ ratios vary from 45 to 161 for apatite from alnöite and jacupirangite (Table 5), whereas ratios range between 106 and 695 for the remaining apatite [14]; these ratios for apatite are generally lower compared to those for perovskite (Table 3).

Figure 8. Chemical variation diagrams for apatite from different rock types (carbonatite (Carb.), alnöite, ijolite, okaite, and jacupirangite (Jac.)). (**A**) Ca^{2+} *vs.* P^{5+}; (**B**) $LREE^{3+}$ *vs.* Si^{4+}. Additional chemical compositions for apatite from carbonatite, okaite and melanite ijolite are from Chen and Simonetti [14].
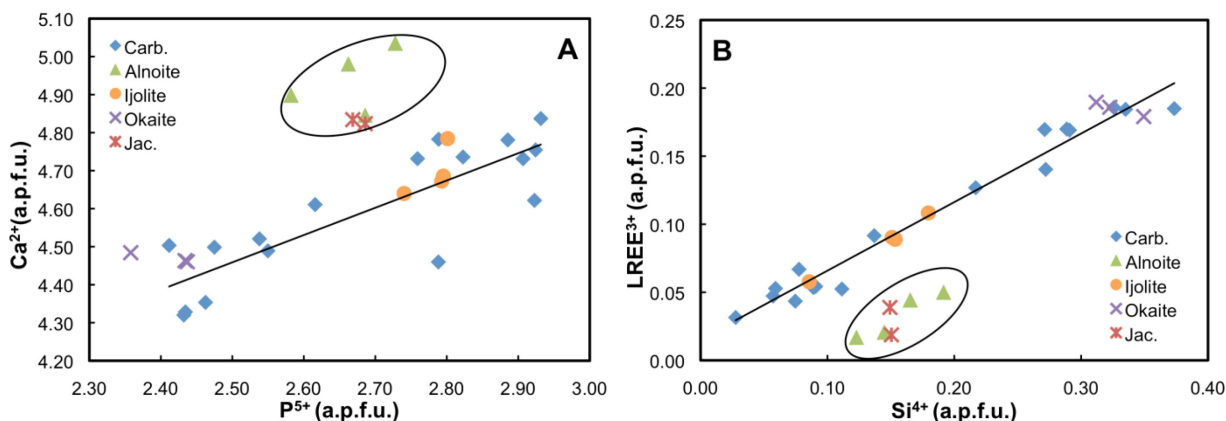
Figure 9. Chondrite normalized REE patterns for apatite from different rock types at Oka. As with Figure 8, additional REE abundances for apatite from carbonatite, okaite and melanite ijolite are from Chen and Simonetti [14]. The grey shaded area outlines the normalized patterns for apatite from alnöite and jacupirangite. Chondrite values are from McDonough and Sun [55].
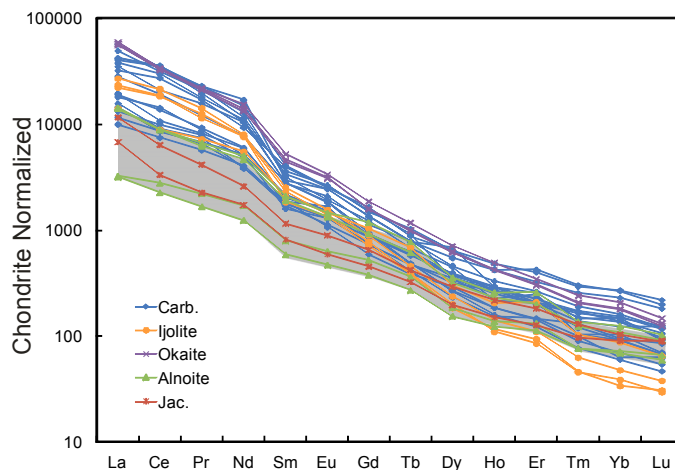

Table 4. Major element abundances of apatite from ijolite, alnöite and jacupirangite.

Sample	Oka132	Oka134	Oka73	Oka75	Oka88	Oka70	Oka78
	alnöite	alnöite	alnöite	alnöite	ijolite	jacupirangite	jacupirangite
	$n = 5$	$n = 10$	$n = 4$	$n = 17$	$n = 9$	$n = 5$	$n = 2$
P_2O_5	37.93	36.47	37.60	38.53	39.56	37.93	37.69
SiO_2	1.73	2.29	1.98	1.47	1.02	1.79	1.80
La_2O_3	0.19	0.48	0.40	0.17	0.54	0.43	0.20
Ce_2O_3	0.27	0.73	0.62	0.20	0.90	0.61	0.29
Pr_2O_3	0.02	0.06	0.14	0.05	0.07	0.03	0.05
Nd_2O_3	0.19	0.38	0.29	0.13	0.38	0.19	0.07
MgO	0.04	0.03	0.03	0.03	0.01	0.02	0.04
CaO	54.07	54.66	55.58	56.19	53.39	53.83	53.95
MnO	0.02	0.01	0.02	0.01	0.05	0.03	0.04
FeO	0.04	0.04	0.03	0.04	0.04	0.13	0.03
SrO	0.48	0.46	0.46	0.47	0.85	0.83	0.52
F	1.77	2.24	2.10	2.05	4.00	2.31	1.93
Total	96.75	97.84	99.24	99.33	100.82	98.15	96.60
P^{5+}	2.686	2.582	2.662	2.728	2.801	2.686	2.668
Ca^{2+}	4.845	4.898	4.980	5.035	4.784	4.824	4.834
Sr^{2+}	0.023	0.022	0.022	0.023	0.041	0.040	0.025
Si^{4+}	0.145	0.192	0.165	0.123	0.086	0.149	0.150
La^{3+}	0.006	0.015	0.012	0.005	0.017	0.013	0.006
Ce^{3+}	0.008	0.022	0.019	0.006	0.028	0.019	0.009
Pr^{3+}	0.001	0.002	0.004	0.002	0.002	0.001	0.002
Nd^{3+}	0.006	0.011	0.009	0.004	0.011	0.006	0.002
$LREE^{3+}$	0.021	0.050	0.044	0.017	0.058	0.039	0.019

Notes: Major element compositions are presented in wt %; Structural formulae of apatite are calculated based on 12 atoms of oxygen.

Table 5. Trace element abundances of apatite from ijolite, alnöite and jacupirangite.

Sample	Oka132 alnöite $n = 5$	Oka134 alnöite $n = 10$	Oka73 alnöite $n = 4$	Oka75 alnöite $n = 17$	Oka88 ijolite $n = 9$	Oka70 jacupirangite $n = 5$	Oka78 jacupirangite $n = 2$
Mn	120	163	167	119	358	194	164
Rb	0.26	0.20	b.d.	1.37	b.d.	b.d.	b.d.
Sr	3798	3716	3393	3842	5774	8938	4236
Y	195	358	327	187	256	325	243
Ba	19.80	27.21	28.71	10.19	92.66	32.36	11.83
La	780	3423	3346	763	3361	2772	1624
Ce	1728	5496	5515	1411	5513	3961	2060
Pr	208	623	584	157	677	390	212
Nd	788	2320	2149	572	2540	1201	801
Sm	120	314	285	87	312	173	122
Eu	35.38	82.65	76.00	26.35	82.89	51.03	33.12
Gd	104	238	186	75.15	209	130	90.48
Tb	13.10	28.42	22.19	9.79	24.69	15.16	11.67
Dy	45.59	87.78	77.74	37.85	74.42	71.85	48.47
Ho	7.50	14.02	12.57	6.70	11.23	11.86	8.22
Er	21.14	41.28	31.95	18.09	33.37	29.24	20.35
Tm	1.88	3.37	3.04	1.89	2.54	3.21	2.39
Yb	11.12	20.04	17.54	11.54	14.15	16.73	14.58
Lu	1.46	2.54	2.24	1.63	1.60	2.19	2.23
Pb	2.93	4.69	4.61	3.20	9.79	2.96	2.50
Th	105	240	161	140	600	52.29	59.41
U	20.86	36.87	25.71	22.52	6.73	21.45	11.29
$(La/Yb)_N$	48	116	130	45	161	113	76

Notes: Trace element concentrations are listed in ppm; b.d. = below detection limit.

3.2. Geochronological Data

New, *in-situ* U-Pb ages for apatite are reported here from three alnöites, one ijolite, two okaites, and one jacupirangite (Table 6). As with the *in-situ* U-Pb dating results documented previously for apatite from Oka by Chen and Simonetti [14], the newly obtained ages for several alkaline silicate rock samples also indicate a bimodal distribution (e.g., Oka132 and Oka229; Figure 10B,C). For example, apatite from alnöite sample Oka75 yields bimodal $^{206}Pb/^{238}U$ weighted mean ages of 111.7 ± 3.4 and 131.6 ± 2.4 Ma. In general, samples with only one age peak (*i.e.*, Oka209, Figure 10A) yield a relatively young age.

In total, ~40 U-Pb analyses for perovskite from four okaites and one alnöite obtained here are listed in Table 7. Of interest, U-Pb ages for perovskite from okaite sample Oka229 also yields a bimodal distribution (Figure 10D). Moreover, individual ages correlate with their corresponding chemical compositions, *i.e.*, older perovskites that define a $^{206}Pb/^{238}U$ weighted mean age of 139.4 ± 2.5 Ma are characterized by high Nb_2O_5 contents (Nb-E group), whereas younger perovskites with an age of 115.7 ± 3.9 Ma belong to the Nb-D group (Figure 5). Of note, the young ages for perovskite obtained in this study (Table 4 and Figure 10E) are younger than the previously reported (single) U-Pb age of

131 ± 7 Ma for the same mineral from carbonatite at Oka [13]. Thus, as with the recently published apatite and niocalite ages for Oka [14,15], the U-Pb perovskite ages obtained here also suggest a rather protracted crystallization history for Oka. Of importance, the Th/U ratios for perovskite investigated in this study are all >1 with the highest value up to 31. Chew *et al.* [41] pointed out that using the [208]Pb-correction method in conjunction with determining [208]Pb-[232]Th ages only yields reliable geochronological results when [232]Th/[238]U ratios are <0.5. Consequently, we do not report the [232]Th-[208]Pb ages for perovskite investigated here.

Figure 10. U-Pb isotopic ages for apatite and perovskite from the Oka carbonatite complex. Examples are illustrated for samples with a single age for apatite (**A**) and bimodal age distributions (**B**,**C**). Diagrams (**D**) and (**E**) illustrate examples of perovskite age results, (**D**) gives a bimodal distribution age and (**E**) yields a single young age. All reported uncertainties are at 2σ level as determined by Isoplot [46]. The Mean Square Weighted Deviation (MSWD) is used as a statistical validity of the regression line according to the criteria defined by Wendt and Carl [56].
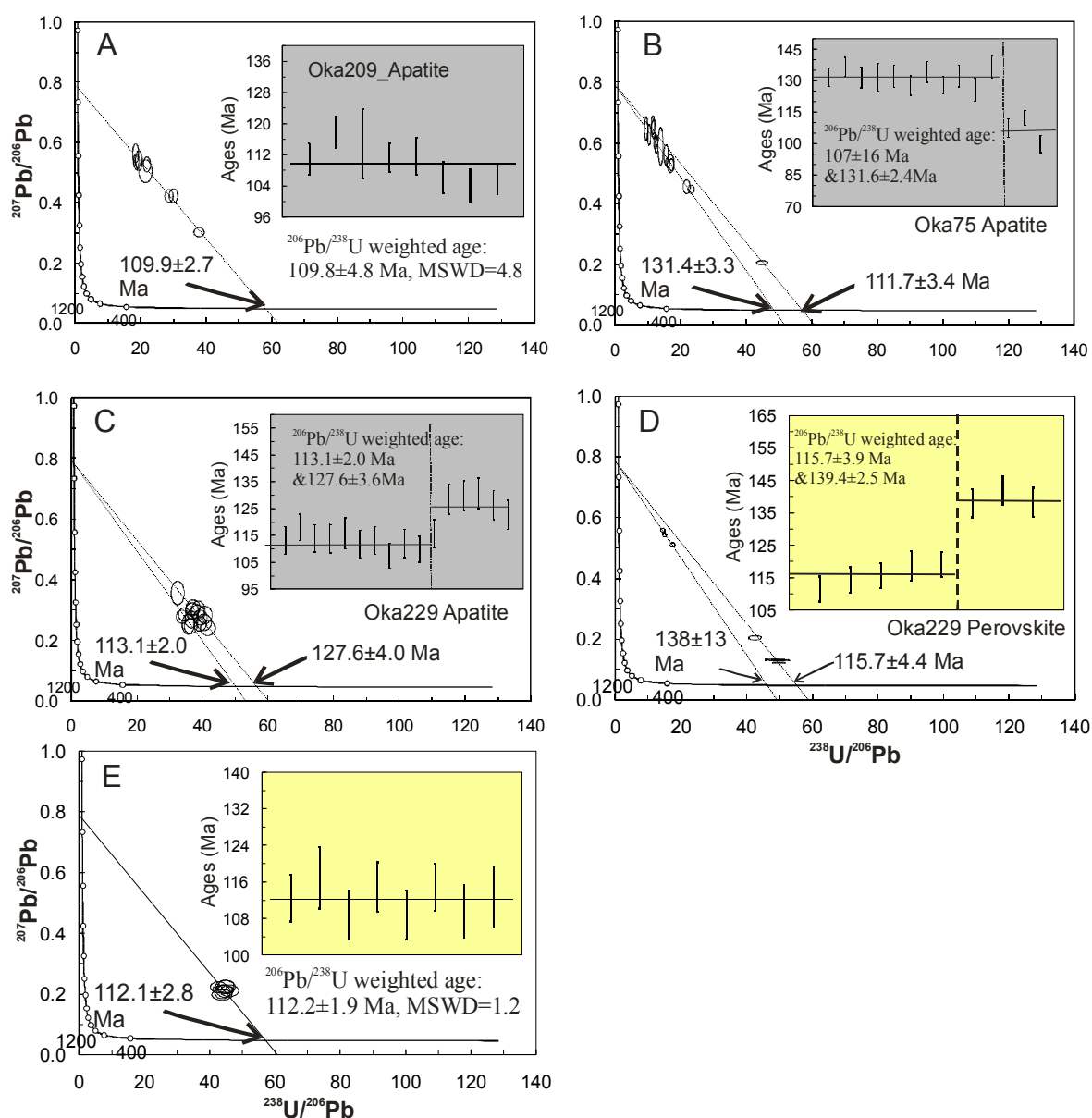
Table 6. *In-situ* U-Pb geochronological results for apatite by LA-ICP-MS. Rad.: Radiogenic.

Analyses	^{206}Pb (cps)	^{238}U (cps)	^{238}U/^{206}Pb	2σ	^{207}Pb/^{206}Pb	2σ	F206	Rad. ^{206}Pb/^{238}U	Rad. ^{206}Pb/^{238}U Age (Ma)	2σ
Oka75										
ap2	3860	73,757	17.297	0.581	0.528	0.016	0.35	0.020	130	4
ap5	3846	67,692	16.153	0.531	0.536	0.013	0.34	0.021	135	4
ap6	2005	27,238	12.429	0.474	0.603	0.018	0.25	0.020	129	5
ap7	2118	39,197	17.029	0.874	0.532	0.024	0.35	0.020	130	7
ap8	2793	19,763	9.551	0.395	0.647	0.033	0.19	0.020	129	5
ap12	2241	32,451	12.690	0.448	0.595	0.025	0.26	0.021	132	5
ap13	3514	93,575	23.239	0.786	0.447	0.011	0.46	0.020	127	4
ap16	2105	51,591	21.907	0.857	0.455	0.019	0.45	0.021	131	5
ap17	1034	16,038	13.968	0.601	0.589	0.051	0.27	0.019	124	5
ap18	1542	17,890	10.492	0.402	0.627	0.028	0.22	0.021	134	5
ap10	2247	31,047	11.825	0.485	0.646	0.025	0.19	0.016	105	4
ap11	8678	436,411	44.920	1.414	0.205	0.006	0.79	0.018	112	4
Oka132										
ap1	2987	42,448	12.778	0.613	0.618	0.037	0.23	0.018	116	6
ap2	2542	26,579	9.461	0.486	0.660	0.045	0.18	0.019	118	6
ap3	4431	120,443	24.373	0.858	0.452	0.017	0.46	0.019	119	4
ap4	4405	127,135	26.202	1.067	0.414	0.017	0.51	0.019	124	5
ap6	5230	136,876	23.515	0.833	0.448	0.017	0.46	0.020	125	4
ap7	5770	123,850	22.334	1.045	0.473	0.023	0.43	0.019	122	6
ap8	4040	107,693	24.499	0.891	0.469	0.035	0.43	0.018	113	4
ap9	6320	213,332	31.331	1.108	0.331	0.014	0.62	0.020	126	4
ap10	4256	111,559	24.952	1.074	0.417	0.024	0.50	0.020	129	6
ap12	4215	127,533	28.325	1.113	0.411	0.016	0.51	0.018	115	5
ap13	2014	39,761	18.813	1.039	0.513	0.029	0.37	0.020	127	7
ap15	4526	134,623	27.585	0.916	0.402	0.015	0.52	0.019	121	4
ap16	5532	182,371	29.898	1.000	0.362	0.016	0.58	0.019	123	4
ap17	4954	134,766	24.557	0.859	0.426	0.019	0.49	0.020	128	4
ap18	5098	140,484	25.011	1.026	0.431	0.016	0.48	0.019	124	5
ap19	4482	118,700	24.078	0.896	0.440	0.019	0.47	0.020	125	5
ap20	4578	117,506	23.534	0.935	0.455	0.020	0.45	0.019	123	5
ap21	4537	126,595	25.390	0.899	0.402	0.017	0.52	0.021	131	5
Oka134										
ap3	2633	46,091	11.623	0.512	0.632	0.033	0.21	0.018	117	5
ap4	2047	57,963	31.557	1.069	0.337	0.011	0.61	0.019	124	4
ap6_2	1881	48,510	12.961	0.513	0.613	0.024	0.24	0.018	118	5
ap7	2226	63,035	12.111	0.460	0.620	0.028	0.23	0.019	121	5
ap8	4950	220,877	26.580	1.025	0.450	0.019	0.46	0.017	110	4
ap10	3204	96,354	36.193	1.188	0.306	0.008	0.65	0.018	115	4

Table 6. *Cont.*

Analyses	^{206}Pb (cps)	^{238}U (cps)	$^{238}U/^{206}Pb$	2σ	$^{207}Pb/^{206}Pb$	2σ	F206	Rad. $^{206}Pb/^{238}U$	Rad. $^{206}Pb/^{238}U$ Age (Ma)	2σ
Oka78										
ap1	2515	44,472	15.505	0.655	0.576	0.031	0.29	0.019	119	5
ap2	2419	36,383	13.013	0.545	0.636	0.033	0.21	0.016	102	4
ap2_2	2682	49,979	15.883	0.719	0.590	0.018	0.27	0.017	109	5
ap5	3147	36,786	10.981	0.475	0.616	0.041	0.23	0.021	136	6
ap6	2235	26,384	9.809	0.432	0.650	0.038	0.19	0.019	123	5
ap7	2127	25,446	10.862	0.638	0.629	0.050	0.22	0.020	127	7
ap8	3479	86,154	20.688	0.770	0.472	0.016	0.43	0.021	132	5
Oka88										
ap1	1928	24,364	10.634	0.571	0.630	0.034	0.22	0.020	130	7
ap5	3191	52,289	14.240	0.526	0.599	0.023	0.26	0.018	116	4
ap9	2266	22,820	8.590	0.379	0.671	0.029	0.16	0.019	119	5
ap12	2087	28,603	11.739	0.460	0.639	0.034	0.20	0.017	111	4
Oka209										
ap1	3806	136,013	28.715	1.044	0.423	0.017	0.50	0.017	110	4
ap2	2669	61,596	18.711	0.627	0.537	0.022	0.34	0.018	116	4
ap3	2792	82,285	21.569	1.675	0.505	0.031	0.38	0.018	114	9
ap5	5696	262,191	37.865	1.239	0.302	0.013	0.66	0.017	111	4
ap6	2535	61,132	19.526	0.857	0.540	0.027	0.34	0.017	110	5
ap7	2545	55,895	18.549	0.728	0.564	0.026	0.30	0.016	105	4
ap8	2418	63,624	21.972	0.892	0.527	0.020	0.35	0.016	103	4
ap9	2622	93,867	30.042	1.094	0.423	0.019	0.49	0.016	105	4

Table 7. *In-situ* U-Pb geochronological results for perovskite by LA-(MC)-ICP-MS.

Analyses	^{206}Pb (V)	^{238}U (V)	$^{238}U/^{206}Pb$	2σ	$^{207}Pb/^{206}Pb$	2σ	F206	Rad. $^{206}Pb/^{238}U$	Rad. $^{206}Pb/^{238}U$ Age (Ma)	2σ
Oka229										
PV1	0.0014	0.075	51.008	1.791	0.130	0.001	0.89	0.017	111	4
PV1_2	0.0012	0.065	49.588	1.661	0.132	0.001	0.89	0.018	114	4
PV2_1	0.0016	0.029	17.390	0.569	0.511	0.005	0.38	0.022	138	5
PV2_2	0.0012	0.064	49.735	1.689	0.122	0.001	0.90	0.018	116	4
PV2_3	0.0011	0.049	42.489	1.631	0.205	0.006	0.79	0.019	119	5
PV2_4	0.0010	0.052	47.546	1.537	0.133	0.001	0.89	0.019	119	4
PV2_5	0.0014	0.022	14.934	0.470	0.544	0.006	0.33	0.022	142	4
PV2_6	0.0013	0.020	14.402	0.470	0.558	0.006	0.31	0.022	138	5
Oka208										
PV1	2,006	90,727	44.557	2.004	0.209	0.016	0.78	0.018	112	5
PV2	2,127	92,231	43.726	2.517	0.198	0.014	0.80	0.018	117	7
PV3	1,928	89,696	45.028	2.215	0.223	0.018	0.76	0.017	108	5
PV4	2,163	92,836	42.614	2.005	0.223	0.015	0.76	0.018	115	5
PV5	2,329	104,011	46.008	2.261	0.211	0.016	0.78	0.017	108	5
PV6	2,079	91,906	43.869	1.961	0.207	0.018	0.79	0.018	115	5
PV7	2,130	94,597	44.558	2.351	0.225	0.017	0.76	0.017	109	6
PV7_2	2,137	96,161	44.041	2.579	0.216	0.011	0.77	0.018	112	7

Table 7. *Cont.*

Analyses	^{206}Pb (V)	^{238}U (V)	^{238}U/^{206}Pb	2σ	^{207}Pb/^{206}Pb	2σ	F206	Rad. ^{206}Pb/^{238}U	Rad. ^{206}Pb/^{238}U Age (Ma)	2σ
Oka209										
PV2	0.0004	0.017	38.887	1.274	0.244	0.003	0.74	0.019	121	4
PV2_2	0.0004	0.019	48.124	1.593	0.159	0.002	0.85	0.018	113	4
PV3	0.0006	0.029	48.942	1.685	0.144	0.002	0.87	0.018	114	4
PV3_2	0.0006	0.033	50.112	1.714	0.140	0.002	0.88	0.017	112	4
PV4	0.0006	0.028	47.879	1.605	0.147	0.002	0.87	0.018	116	4
PV4_2	0.0006	0.030	43.947	1.397	0.189	0.003	0.81	0.018	118	4
PV5	0.0006	0.028	44.530	1.509	0.162	0.002	0.85	0.019	121	4
PV5_2	0.0006	0.028	44.981	1.481	0.158	0.002	0.85	0.019	121	4
Oka137										
PV1	0.0009	0.042	45.790	1.615	0.165	0.002	0.84	0.018	118	4
PV1_2	0.0012	0.018	13.855	0.500	0.560	0.006	0.31	0.022	143	5
PV3	0.0012	0.019	14.283	0.478	0.552	0.006	0.32	0.022	143	5
PV3_2	0.0011	0.017	14.344	0.464	0.559	0.006	0.31	0.022	138	4
PV4	0.0010	0.020	18.015	0.587	0.504	0.005	0.39	0.021	137	4
PV4_2	0.0011	0.020	17.352	0.636	0.517	0.005	0.37	0.021	135	5
PV5	0.0011	0.028	23.512	0.936	0.427	0.005	0.49	0.021	133	5
PV5_2	0.0009	0.041	42.112	1.336	0.228	0.004	0.76	0.018	115	4
Oka73										
PV3	0.0009	0.039	39.781	1.357	0.235	0.003	0.75	0.019	120	4
PV4	0.0014	0.027	17.431	0.686	0.515	0.005	0.37	0.021	136	5
PV7	0.0006	0.028	42.803	1.349	0.148	0.002	0.87	0.020	129	4
PV7_2	0.0007	0.033	45.200	1.532	0.160	0.002	0.85	0.019	120	4
PV8	0.0021	0.059	26.176	1.013	0.395	0.007	0.53	0.020	130	5
PV9	0.0018	0.093	50.231	1.697	0.123	0.002	0.90	0.018	115	4

Notes: F206 is the proportion of common ^{206}Pb; Sample Oka208 is determined by LA-ICP-MS, and all other samples are analyzed by LA-MC-ICP-MS. Rad.: Radiogenic.

A recent geochronological study by Chen *et al.* [15] focused on the Nb-disilicate mineral, niocalite, for which Oka is the type locality. Niocalite from one of the carbonatite samples investigated by Chen *et al.* [15] also indicates a bimodal age distribution with weighted mean ^{206}Pb/^{238}U ages of 110.1 ± 5.0 and 133.2 ± 6.1 Ma, and overlaps that of co-existing apatite for the same sample [15]. Niocalite from two other carbonatite samples yield younger ages of 110.6 ± 1.2 and 115.0 ± 1.9 Ma [15].

In summary, a total of 293 *in-situ* U-Pb apatite ages yield a bimodal distribution pattern using the Kernel Density Estimation (KDE) diagram (Figure 11A; KDE is a standard statistical technique used for estimating the density distribution in geochronlogical studies) [57], with two peaks at ~126 and ~115 Ma. The variable perovskite ages indicate an additional older age peak at 135.4 ± 3.2 Ma (Figure 11D), which is similar (given the associated uncertainties) to the age of 131 ± 7 Ma for perovskite obtained by Cox and Wilton [13]. In contrast, the niocalite U-Pb dating results tend to converge toward the younger age, with a peak at 112.6 ± 1.2 Ma (Figure 11C) [15]. The majority of the combined *in situ* U-Pb dating results for apatite, perovskite, and niocalite from Oka clearly support a protracted history of magmatic activity in the order of ~10–15 million years (Figure 11A).

Figure 11. Kernel Density Estimation (KDE) plots for the weighted mean $^{206}Pb/^{238}U$ ages for the different rock/mineral groups. (**A**) The entire geochronological data for Oka (*n* = 363); (**B**) apatite (*n* = 293); (**C**) niocalite (*n* = 38); (**D**) perovskite (*n* = 32); (**E**) carbonatite (*n* = 160); (**F**) okaite (*n* = 101); (**G**) ijolite (*n* = 44); (**H**) alnöite (*n* = 41).
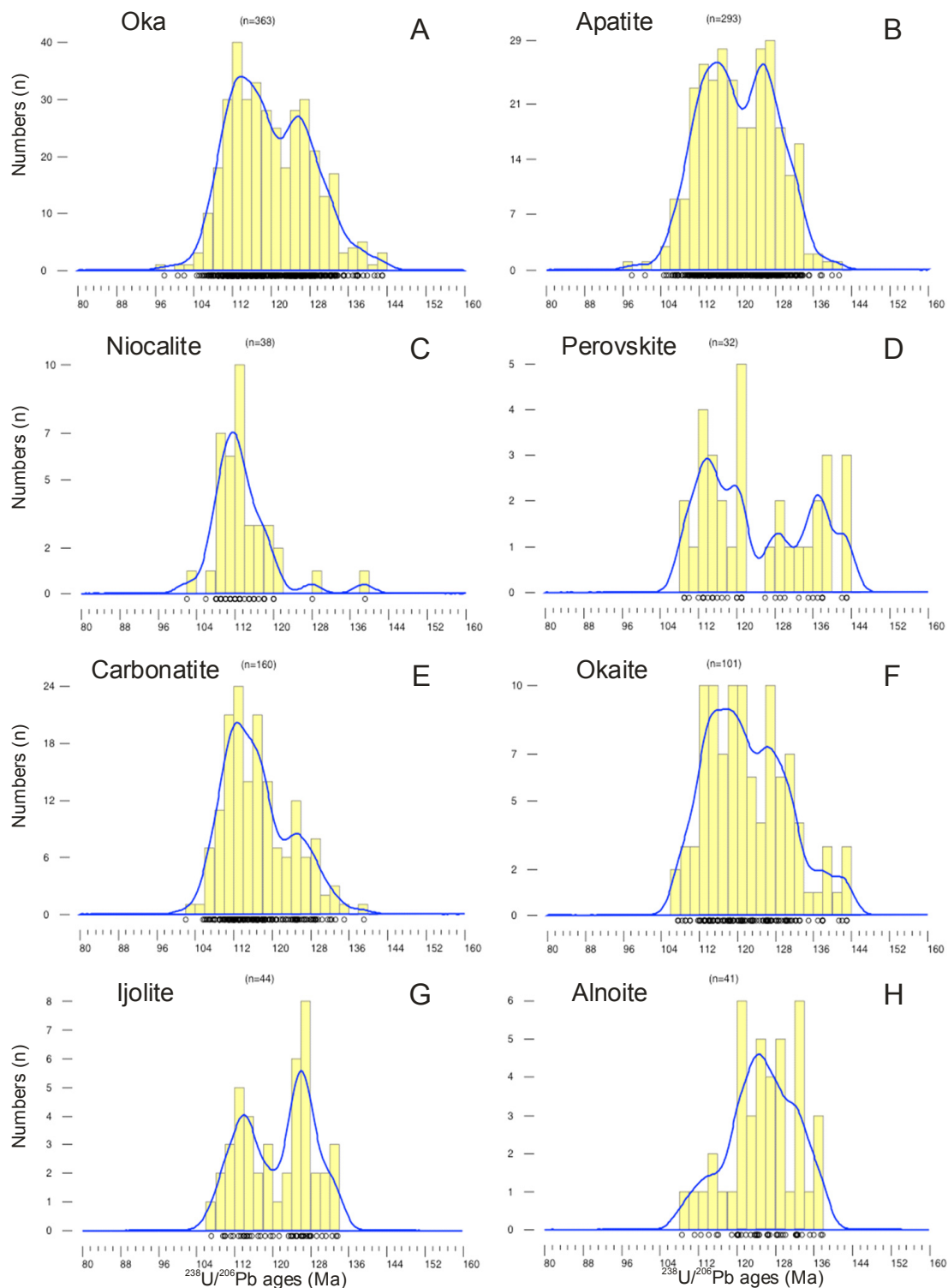
3.3. Radiogenic Isotope Data

The Sr and Nd isotope results for perovskite and apatite obtained here are listed in Table 8 and shown in Figure 12. Overall, Rb concentrations are below (or close to) the detection limit, and

consequently the calculated Rb/Sr ratios are extremely low so that the age correction of the measured $^{87}Sr/^{86}Sr$ ratio is negligible. For the Sm-Nd data, a correction for radiogenic ^{143}Nd was applied, and ages used for the correction were based on the U/Pb dating results obtained here. The *in-situ* Sr and Nd isotope data for both perovskite and apatite overlap the entire range defined by previously reported whole rock data for carbonatite from Oka [12], but definitely indicate a larger variation ($^{87}Sr/^{86}Sr$: 0.70312–0.70367; $^{143}Nd/^{144}Nd$: 0.51270–0.51286), and is not consistent with closed-system behavior (Figure 12A). Of interest, the Nd and Sr isotope data from Oka overlap the upper end of the East African Carbonatite Line (EACL; Figure 12B) [58]. The EACL is defined by the Nd-Sr isotope values for young (<40 Ma old) East African carbonatites, and was interpreted to represent mixing between two end-member mantle components: HIMU (mantle component with time integrated, high $^{238}U/^{204}Pb$ ratio)- and EMI (enriched mantle 1)-like.

Figure 12. (**A**) Diagram of $^{143}Nd/^{144}Nd$ *vs.* $^{87}Sr/^{86}Sr$ shows data obtained in this study and by Wen *et al.* [12]. (**B**) Plot of $^{143}Nd/^{144}Nd$ *vs.* $^{87}Sr/^{86}Sr$. Also shown are the East African Carbonatite Line (EACL) from Bell and Blenkinsop [58], and CHUR and Bulk Earth (BE) values for comparison. (**C**) Diagram of $^{143}Nd/^{144}Nd$ *vs.* $^{87}Sr/^{86}Sr$ values for the different groups of perovskite.
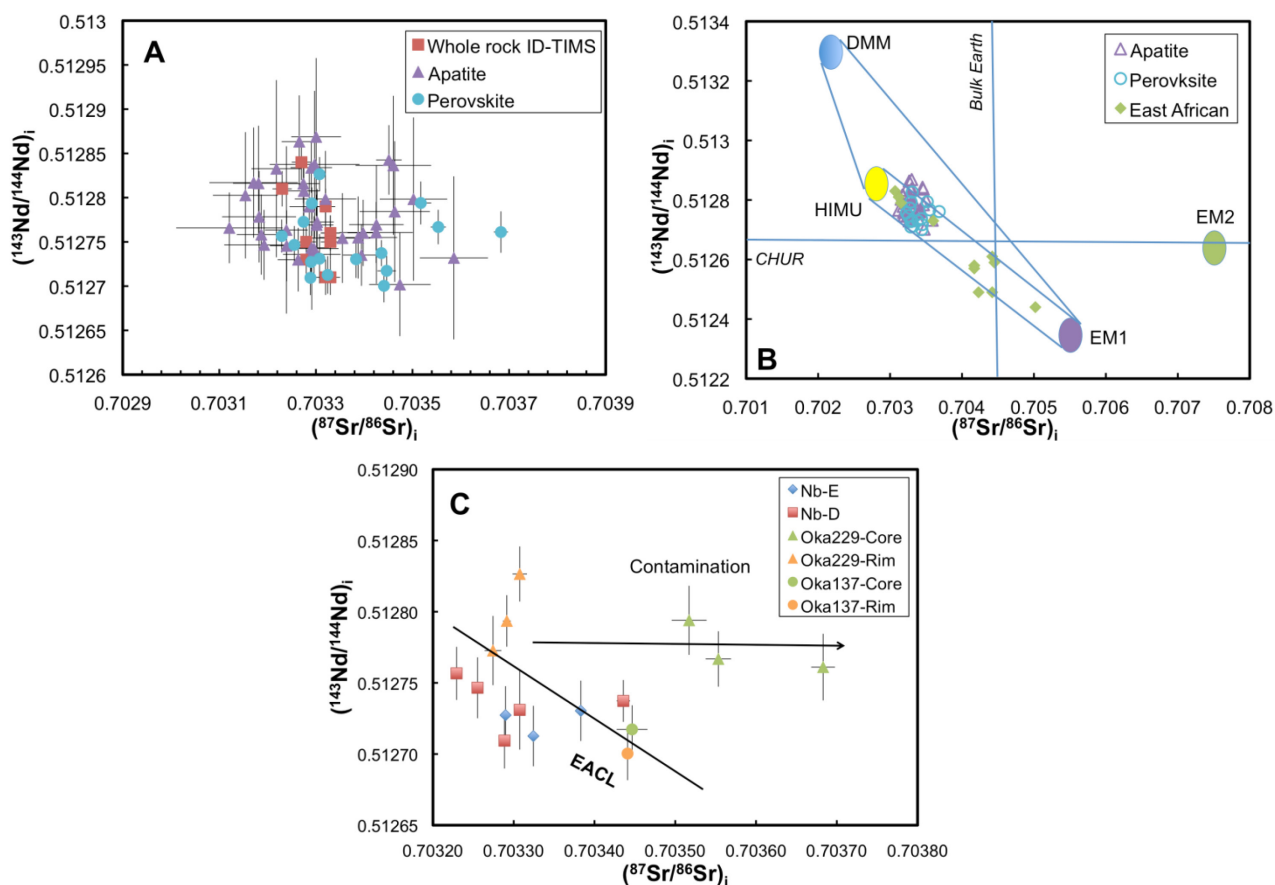
Table 8. *In-situ* Sr and Nd isotopic compositions for perovskite and apatite by LA-MC-ICP-MS.

Sample	Analysis	$(^{87}Sr/^{86}Sr)_i$	2σ	$^{143}Nd/^{144}Nd$	$(^{143}Nd/^{144}Nd)_i$	2σ
Oka4b	AP1	0.70327	0.00004	0.51283	0.51279	0.00004
	AP7	0.70326	0.00004	0.51277	0.51273	0.00004
	AP12	0.70330	0.00003	0.51281	0.51277	0.00004
Oka51	AP1	0.70329	0.00006	0.51279	0.51274	0.00006
	AP5	0.70330	0.00005	0.51292	0.51287	0.00009
	AP8	0.70343	0.00006	0.51282	0.51277	0.00007
	AP14	0.70319	0.00005	0.51281	0.51276	0.00005
Oka72	AP2	0.70349	0.00003	0.51275	0.51270	0.00018
	AP17	0.70346	0.00007	0.51283	0.51278	0.00008
Oka153	AP22	0.70345	0.00003	0.51277	0.51272	0.00003
Oka200a	AP6	0.70322	0.00005	0.51288	0.51283	0.00010
	AP12	0.70350	0.00008	0.51284	0.51275	0.00013
Oka206	AP1	0.70327	0.00003	0.51285	0.51281	0.00003
	AP13_1	0.70329	0.00004	0.51287	0.51283	0.00003
Oka21	AP10	0.70332	0.00006	0.51284	0.51280	0.00005
	AP11	0.70315	0.00007	0.51285	0.51280	0.00007
	AP14	0.70330	0.00009	0.51288	0.51284	0.00008
Oka31	AP1	0.70329	0.00004	0.51285	0.51281	0.00004
	AP5	0.70324	0.00003	0.51281	0.51276	0.00004
	AP7	0.70330	0.00003	0.51283	0.51279	0.00004
	AP11	0.70327	0.00003	0.51279	0.51275	0.00004
	AP12	0.70329	0.00004	0.51281	0.51277	0.00003
Oka89	AP2	0.70359	0.00007	0.51277	0.51273	0.00009
	AP3	0.70347	0.00006	0.51274	0.51270	0.00006
	AP9	0.70346	0.00008	0.51288	0.51284	0.00008
Oka138	AP4	0.70340	0.00003	0.51281	0.51276	0.00004
	AP6	0.70330	0.00005	0.51279	0.51274	0.00004
	AP7	0.70339	0.00004	0.51278	0.51274	0.00003
	AP13	0.70339	0.00008	0.51280	0.51275	0.00005
	AP14	0.70342	0.00008	0.51281	0.51276	0.00003
	AP19	0.70335	0.00006	0.51280	0.51275	0.00005
Oka229	AP7	0.70319	0.00008	0.51280	0.51275	0.00004
	AP18	0.70318	0.00008	0.51283	0.51278	0.00005
	AP19	0.70312	0.00011	0.51282	0.51277	0.00004
	AP20	0.70317	0.00009	0.51286	0.51282	0.00006
Oka75	AP8	0.70336	0.00004	0.51279	0.51272	0.00016
	AP12	0.70349	0.00005	0.51278	0.51271	0.00021
	AP13	0.70342	0.00005	0.51290	0.51283	0.00007
Oka132	AP8	0.70353	0.00007	0.51287	0.51280	0.00013
	AP9	0.70350	0.00007	0.51286	0.51280	0.00009
	AP10	0.70364	0.00008	0.51299	0.51293	0.00016
	AP18	0.70367	0.00006	0.51288	0.51282	0.00013

<div align="center">**Table 8.** *Cont.*</div>

Sample	Analysis	(^{87}Sr/^{86}Sr)$_i$	2σ	^{143}Nd/^{144}Nd	(^{143}Nd/^{144}Nd)$_i$	2σ
Oka137	PV1_1	0.70345	0.00002	0.51277	0.51272	0.00002
	PV1_2	0.70344	0.00001	0.51275	0.51270	0.00002
	PV3_2	0.70338	0.00001	0.51277	0.51273	0.00002
	PV4_2	0.70332	0.00000	0.51276	0.51271	0.00002
	PV5	0.70329	0.00000	0.51277	0.51273	0.00002
	PV5_2	0.70344	0.00001	0.51278	0.51274	0.00001
Oka209	PV2_1	0.70323	0.00000	0.51281	0.51276	0.00002
	PV2_2	0.70326	0.00001	0.51280	0.51275	0.00002
	PV4	0.70329	0.00000	0.51276	0.51271	0.00002
	PV5	0.70331	0.00001	0.51279	0.51273	0.00003
Oka229	PV2_1	0.70329	0.00000	0.51284	0.51279	0.00002
	PV2_2	0.70352	0.00002	0.51285	0.51279	0.00002
	PV2_3	0.70355	0.00002	0.51282	0.51277	0.00002
	PV2_4	0.70368	0.00001	0.51281	0.51276	0.00002
	PV2_5	0.70327	0.00001	0.51282	0.51277	0.00002
	PV2_6	0.70331	0.00001	0.51287	0.51283	0.00002

<div align="center">Notes: AP = apatite; PV = perovskite.</div>

4. Discussions

4.1. Timing of Magmatism at Oka

The timing of magmatism associated with the Oka carbonatite complex was previously investigated by apatite fission track, *in-situ* U-Pb dating for apatite, niocalite, and a single perovskite age determination [13–15]. All the data from these previous geochronological studies are indicative of a protracted petrogenetic history with a duration in the order of ~10–15 million years (given the associated uncertainties). However, this study is the first to report a thorough *in-situ* U-Pb geochronological investigation for apatite and perovskite from the associated silica-undersaturated rocks at Oka, *i.e.*, ijolite, alnöite, and jacupirangite.

Based on the geochronological data shown in Figure 11, it is clear that all the rock types display a protracted crystallization history (Figure 11A); however, their respective age distribution patterns vary slightly. U-Pb dating results for alnöite are shifted slightly towards the older ages with the majority falling between ~124 and ~135 Ma, and a minor peak at ~115 Ma (Figure 11H). In contrast, a majority of the U-Pb ages for carbonatite yield a younger age signature with the main peak at ~114 Ma, and a minor older peak at ~126 Ma (Figure 11E). The ages for okaite are more evenly distributed and vary between ~114 and ~127 Ma (Figure 11F). The U-Pb dating results for ijolite define the most distinctive bimodality with two peaks at ~114 and ~127 Ma (Figure 11G). Thus, the older age peak for perovskite at 135.4 ± 3.2 Ma and the younger niocalite age at 112.6 ± 1.2 Ma may define the absolute "maximum" duration of magmatism at Oka.

Overall, the magmatic history for Oka may be summarized as follows: (1) An early igneous event occurred at ~135 Ma, which corresponds to the main period of formation for the alkaline silicate rocks, in particular the alnöite and ijolite; (2) This was followed by the main period of emplacement for

okaite between 120 and 127 Ma; and (3) Lastly, at ~114 Ma, emplacement of the vast majority of the carbonatite, along with okaite, ijolite, and a minor amount of alnöite occurred.

Oka is not the sole alkaline complex that is characterized by an extended formational history spanning millions of years. Several previous studies of carbonatite and kimberlite alkaline complexes also define a protracted history of magmatic activity up to 40 million years [36,59–67]. Of note, based on U-Pb ages for ~30 kimberlite complexes in North America, Heaman and Kjarsgaard [59] stated that discrete kimberlite emplacement events within individual fields can occur over time intervals of up to 20 Myrs. For example, the majority of the kimberlite complexes located within the region of Timiskaming, which is located ~1000 km northwest from the MIP, were emplaced between 155 and 134 Ma (*i.e.*, over ~20 Myrs period).

The protracted emplacement history (and ensuing melt differentiation) that occurred at Oka may be explained by invoking either one of two models: (1) Melt generation occurred at ~135 Ma, followed by magma differentiation in a closed-system over a period of ~10–15 million years; or (2) There was periodic generation of small volume, partial melts from a metasomatized, CO_2-bearing mantle source over a period ~10–15 million years, with each melt fraction undergoing an independent crystallization/differentiation path. Given the extremely large variations in trace element abundances recorded by apatite (Table 5) [14], and those depicted by perovskite investigated here (Figures 4–7; Tables 2 and 3), it is difficult if not impossible to attribute these variations to closed-system melt differentiation involving solely one parental melt, regardless of whether this melt was carbonatitic, or a carbonate-rich, alkaline, silica-undersaturated parental melt [14]. Chen and Simonetti [14] advocated for open-system behavior, possibly involving magma mixing, which is an interpretation also put forward by Zurevinski and Mitchell [68] to explain the chemical variations documented by pyrochlore from Oka. In this study, Figures 8 and 9 (and Tables 4 and 5) clearly indicate that the chemical compositions for apatite from alnöite and jacupirangite are distinct relative to those from other rock types. Their major and trace element contents and REE chondrite normalized patterns suggest derivation from a different mantle source. Of interest, Nb-E perovskites are only present in okaite and some represent the rim of zoned perovskite grains (Figure 5). The latter texture has been described as reverse zoning (*i.e.*, an increase of REE and Th contents from core to rim) [53], which is uncommon and possibly results from re-equilibration of perovskite with magma modified by assimilation or contamination processes, or later surrounded by a melt of different composition [53]. Thus, based on the combined chemical and geochronological data obtained for all rock types at Oka, we believe that the second hypothesis involving periodic generation of small volume melts and subsequent magma mixing best explains the petrogenetic history of the complex.

4.2. Relationship between Oka, Monteregian Igneous Province (MIP)-Related Intrusions, and Mantle Plumes?

There exist two competing hypotheses for the formation of Oka and the associated MIP-related intrusions in southeastern Québec (Figure 1A). One model proposes that they formed as the result of intraplate melting in an extensional setting associated with opening of the Atlantic Ocean [69,70]. The alternative view is that the MIP results from the passage of the North American plate over the Great Meteor hotspot [59,71–74]. The main criticism with the latter is the lack of a precise correlation

between the radiometric ages of the MIP-related intrusions and lithospheric plate migration (*i.e.*, geographic position). However, the majority of the geochronological data for the MIP-related intrusions were obtained either by apatite fission-track or K-Ar methods, and only a small number of analyses were conducted for each intrusion. Thus, a more thorough and robust geochronological evaluation is required for each of the MIP intrusions before the plume hypothesis is completely ruled out. Moreover, the results from this study and Chen and Simonetti [14] both report ages for Oka that overlap the entire MIP age range, which further complicate matters in relation to evaluating a temporal relationship for the MIP intrusions relative to a plume hypothesis.

Carbonatites can provide valuable information for deciphering the geochemical nature of the upper mantle as their isotopic ratios inherited from their source region are buffered against crustal contamination due to their extremely high concentrations of incompatible elements (e.g., Sr and Nd). For example, in their study of the carbonatites and associated Si-undersaturated rocks from the Chilwa Island carbonatite complex, Simonetti and Bell [75] clearly indicate that an unrealistic amount of crustal assimilation is needed in order to explain the variable Nd and Sr isotope ratios. Hence, they advocated for melt derivation from a chemically and isotopically heterogeneous (metasomatized) mantle source region. In this study, the Nd and Sr isotope data for both apatite and perovskite overlap those previously obtained for whole rock samples from Oka (Figure 12) [12], but the former are clearly much more variable. This simply reflects the fact that whole rock analyses represent a weighted average of the Sr and Nd isotope composition of the (Sr- and Nd-bearing) constituent minerals (e.g., apatite, calcite, perovskite, and niocalite), and mask subtle differences between phases; however, the latter provide important details for deciphering the petrogenetic history of a complex. Evidence for "open-system" behavior at Oka was already evident from the TIMS generated whole rock data as these define a range of Sr and Nd isotope values that are well outside the typical in-run analytical precision (Figure 12). In Figure 12B, the Nd and Sr isotope compositions for apatite and perovskite from Oka are compared to those for well-established mantle components (*i.e.*, HIMU, EMI, EMII (enriched mantle 2), and DMM (depleted mid-ocean ridge basaltic mantle)) [76] and East African carbonatite complexes [58]. The Nd and Sr isotope data from Oka plot proximal to the field for the HIMU mantle component and most lie along a HIMU-EMI mixing array. Both HIMU and EMI are prevalent mantle components that underlie most of East Africa and also characterize the isotope compositions of ocean island basalts (OIBs) worldwide. Several previous investigations have advocated for the involvement of HIMU, EMI, and FOZO (Focus Zone) mantle components in the generation of most young (<200 Ma) carbonatites on a global scale [77–81]. On the basis of a compilation of both radiogenic and stable isotopic data from carbonatites worldwide, Bell and Simonetti [82] made the argument that parental carbonatitic magmas are derived from a sub-lithospheric source that is associated with either asthenospheric "upwellings" or more deep-seated, plume-related activity. Amongst the important evidences that support the generation of carbonated melts from sub-lithospheric mantle are: the petrogenetic and temporal association of carbonatites with large igneous provinces (LIPs; e.g., Deccan, Parana), carbonatites with primitive noble gas isotopic signatures, and their radiogenic isotope ratios similar to OIBs.

Numerous previous studies have advocated for a direct link between carbonatite melt generation and mantle plumes [74,78,82,83]. As pointed out by Rukhlov and Bell [9], the presence of carbonatites may mark the initiation of mantle-generated magmatism because of the very fluid nature of carbonatitic

melts, and the fact that they are produced by low degrees of partial melting (*i.e.*, precursors to basaltic activity, and perhaps are associated with changes in mantle dynamics). In relation to the southeastern region of Québec and location of the MIP intrusions, tomographic data clearly indicates the presence of a low-velocity anomaly in the upper mantle region beneath the Ottawa-Bonnechere Rift [84]. This anomaly is further interpreted to extend over a broad region at a depth of ~200 km beneath the Great Lakes, where lithosphere was partially breached by the Great Meteor plume [85]. Hence, in relation to the MIP-related magmatism, we propose that carbonatite-like melts and volatile-bearing fluids first metasomatized the upper mantle at ~135 Ma, which gave rise to the older alkaline silicate rocks at Oka (e.g., alnöite). Subsequently, based on the limited geochronological data for the remaining MIP-related intrusions (Table 9) [16,86], the slightly undersaturated to critically saturated complexes of Mounts Royal, Bruno, Rougemont, Yamaska, Shefford, and Brome were emplaced between ~135 Ma and ~128 Ma. The last magmatism to occur involved generation of the moderately-to-strongly undersaturated silicate melts at Royal, Johnson, Yamaska, Shefford, and Brome that occurred ~117 Ma.

Table 9. Ages for Monteregian Intrusions.

Intrusion	Rock type/phase	Mineral dated	Method	Age	2σ
Royal	Nepheline diorite	Sphene	Fission track	117	3
	Leucogabbro	Apatite	Fission track	138	6
	Pyroxenite	Apatite	Fission track	134	9
Bruno	Gabbro	Apatite	Fission track	135	11
	Pyroxenite	Apatite	Fission track	135	11
Johnson	Essexite	Apatite	Fission track	117	9
	Pulaskite	Apatite	Fission track	120	8
Rougemont	Gabbro	Apatite	Fission track	136	10
	Pyroxenite	Apatite	Fission track	138	11
Yamaska	Essexite	Apatite	Fission track	119	8
	Nepheline syenite	Sphene	Fission track	120	10
	Younger pyroxenite	Apatite	Fission track	132	10
	Older pyroxenite	Apatite	Fission track	140	9
	Gabbro	Apatite	Fission track	140	11
	Gabbro	Apatite	Fission track	141	9
Shefford	Nordmarkite	Whole-rock isochron	Rb-Sr	120.3	1
	Pulaskite	Whole-rock isochron	Rb-Sr	128.5	3
	Nepheline diorite	Apatite	Fission track	119	8
	Diorite	Apatite	Fission track	131	8
Brome	Nepheline diorite	Whole-rock isochron	Rb-Sr	118.4	2.2
	Pulaskite	Whole-rock isochron	Rb-Sr	136.2	1.7
	Nepheline diorite	Apatite	Fission track	117	9
	Gabbro	Apatite	Fission track	139	13

4.3. Chemical Zoning of Perovskite

Two perovskite grains (from a total of 25) investigated here display reverse zoning, with Nb and REE abundances that are enriched in the rim relative to their respective central regions of the crystals; the latter may have undergone Pb loss since these are characterized by younger ages resulting from

higher U abundances relative to the rim (Figure 5). Minerals yielding younger ages within any given sample should always be carefully examined for Pb loss or U addition, especially since the Nb-D and Nb-E groups of perovskite have different trace element compositions (e.g., Pb, Th; Figure 7 and Tables 2 and 3). Figure 13A plots U-Pb ages against their respective U abundances for perovskite and it is possible that the young ages corresponding to the higher U contents in samples Oka229, Oka73, and Oka137 can be attributed to Pb loss. The reason being that perovskite with higher U abundances (~200 ppm in this case) will undergo a higher amount of alpha decay from the radioactive disintegration of U, which consequently damages the crystal structure; this then enhances the possibility of losing loosely bound radiogenic Pb. In contrast, perovskite from okaite samples Oka208 and Oka209 yield relatively young ages of 112.2 ± 1.9 Ma (Figure 10E) and 116.4 ± 2.9 Ma, respectively, with U contents comparable to those for the older perovskite (Figure 13A). A previous study of perovskite attributed the higher abundances of incompatible elements at grain boundaries to secondary processes; e.g., alteration in intergranular regions as a result of interaction with a melt, an aqueous fluid, or a gas phase [53]. As stated above, the core areas of two large perovskite grains may have undergone a Pb loss event, and these are characterized by more radiogenic Sr (and comparable Nd) isotopic ratios compared to the remaining perovskite (Figure 12C). In addition, the core regions are marked by distinct chemical compositions (*i.e.*, lower Nb/Zr; Figure 14A,B). Hence, the distinct, more radiogenic $^{87}Sr/^{86}Sr$ isotope compositions for the cores of these two perovskite grains may be attributed to either crystallization from a melt derived from a distinct mantle source, or perturbation by a contamination/alteration process (Figures 12C and 14). Thus, a possible formational history for the reversely zoned perovskite grains is as follows: (1) the cores formed from a first batch of magma; (2) this was followed by the influx of a new (distinct) batch of magma with lower $^{87}Sr/^{86}Sr$ ratio (relative to the cores), which resulted in the crystallization of the rims; and (3) the latter was associated with an "autometasomatic" event in which fluids scavenged the Nb (and certain other trace elements) from the core towards the rim. Obviously, this process was not widespread since only two of the perovskite grains investigated here exhibit this anomalous, reversely zoned texture. It is possible that this "autometasomatic" activity produced the vast majority of the late-stage pyrochlore and/or niocalite resulting in the Nb ore deposits at Oka. Chen *et al.* [15] discussed the issue of late-stage replacement of niocalite by pyrochlore (or vice versa) at Oka. In addition, Samson *et al.* [87] also advocated for the occurrence of late-stage hydrothermal activity at Oka as recorded by fluid inclusions within constituent minerals.

The highly variable chemical compositions, Nd and Sr isotope ratios, and ages documented for perovskite, pyrochlore, niocalite, and apatite from the different rock types associated with the Oka carbonatite complex indicate that these formed as a result of episodic, small volume partial melting and subsequent magma mixing [14,15,68]. However, Figure 13B shows that there is a positive correlation between the total REE contents and U-Pb ages for the perovskite grains investigated here (excluding the two reversely zoned grains). Thus, a possible interpretation is that the Nb-E perovskite formed first within a melt produced at ~135 Ma, and their enriched geochemical nature is the result of low-degree partial melting of a metasomatized (carbonated) mantle source region. The Nb-D perovskite formed later at ~114 Ma from a less-enriched magma and possibly reflects derivation from a more depleted (less metasomatized) mantle source region.

Figure 13. (**A**) Plots illustrating the chemical and geochronological data for perovskite: (**A**) U abundances *vs.* $^{206}Pb/^{238}U$ ages; and (**B**) REE contents *vs.* $^{206}Pb/^{238}U$ ages.
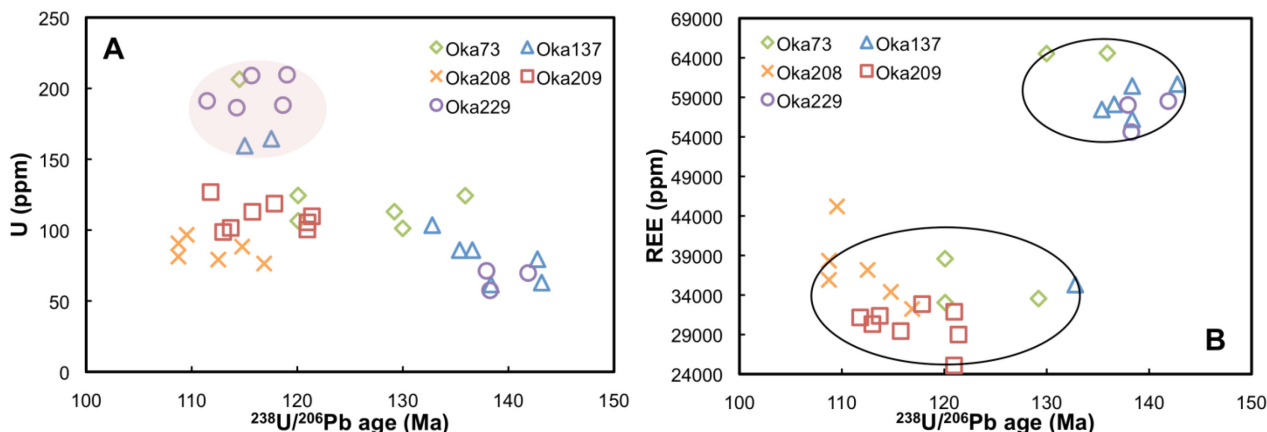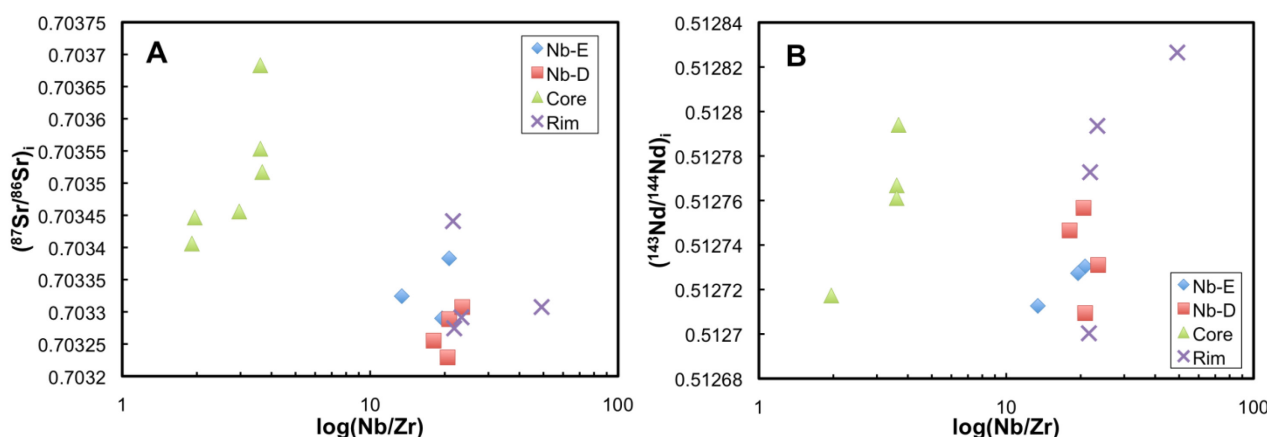

Figure 14. (**A**) Diagram of $^{87}Sr/^{86}Sr$ *vs.* Nb/Zr illustrating the different groups of perovskite; and (**B**) Plot of $^{143}Nd/^{144}Nd$ *vs.* Nb/Zr for the different perovskite groups.

5. Conclusions

This study reports combined geochemical, isotopic, and geochronological data for both perovskite and apatite from the Oka carbonatite complex, and clearly demonstrates that a more detailed petrogenetic history can be deciphered for complexly zoned igneous centers. Of importance, the U-Pb results from this study indicate the need for conducting a thorough geochronological investigation rather than defining the age of any one alkaline intrusive complex solely on the basis of a single or small number of radiometric age determinations.

The combined chemical, isotopic and geochronological data for apatite suggest that its crystallization occurred during the entire magmatic history of the complex. Moreover, the lack of any significant correlations between geochemical and geochronological results for apatite and niocalite indicate a complicated petrogenetic history involving magma mixing [14,15]. On the basis of correlations between chemical compositions and U-Pb ages for the perovskite investigated in this study, these formed during two main episodes of melt generation.

The geochronological results from this study offer valuable insights into the emplacement relationships between carbonatite, okaite, ijolite and alnöite at Oka. It is proposed that carbonatite-like

melts/fluids were the first to emanate from an enriched, volatile-bearing mantle plume, and these interacted with the overlying lithosphere; ensuing alkaline silicate melts were formed and generated the first alnöite, ijolite and okaite emplaced at ~135 Ma. Periodic, small volume partial melting subsequently continued, with a second major pulse of magmatism that occurred at ~114 Ma. Later generation melts mixed with earlier-formed rocks and minerals so as to yield samples with multiple-aged accessory minerals; these are considered as cognate crystals [14]. The Sr and Nd isotopic compositions for perovskite and apatite indicate the involvement of at least two mantle endmembers, HIMU- and EMI-like, within their mantle source region, although dominated by the former component. Given the results reported here and from previous investigations on Oka [14,15], it is difficult to assign either component to a mantle region; *i.e.*, lithosphere *vs.* asthenosphere (or plume). Alternatively, the mantle plume itself may be isotopically heterogeneous as proposed for the magmatic/tectonic regime for the East African alkaline province [58]. Regardless of which model is preferred, infiltration/refertilization of the lithosphere by enriched, volatile-bearing melts/fluids from a plume component will "swamp" the geochemical and isotopic composition of the overlying lithosphere [82].

Acknowledgments

Author Contributions

Wei Chen performed all the analytical work under the supervision of Antonio Simonetti. Wei Chen and Antonio Simonetti participated equally in the interpretation of the data and co-wrote the manuscript.

Conflicts of Interest

The authors declare no conflict of interest.

References

1. Woolley, A.R.; Kjarsgaard, B.A. *Carbonatite Occurrences of the World: Map and Database*; Open File 5796; Natural Resources Canada: Sherbrooke, QC, Canada, 2008.
2. Bizzarro, M.; Simonetti, A.; Stevenson, R.K.; David, J. Hf isotope evidence for a hidden mantle reservoir. *Geology* **2002**, *30*, 771–774.
3. De Moor, J.M.; Fischer, T.P.; King, P.L.; Botcharnikov, R.E.; Hervig, R.L.; Hilton, D.R.; Barry, P.H.; Mangasini, F.; Ramirez, C. Volatile-rich silicate melts from Oldoinyo Lengai volcano (Tanzania): Implications for carbonatite genesis and eruptive behavior. *Earth Planet. Sci. Lett.* **2013**, *361*, 379–390.
4. Bell, K.; Dawson, J.B. Nd and Sr isotope systematics of the active carbonatite volcano, Oldoinyo Lengai. In *Carbonatite Volcanism: Oldoinyo Lengai and the Petrogenesis of Natrocarbonatites*; Bell, K., Keller, J., Eds.; Springer: Berlin, Germany, 1995; pp. 100–112.

5. Dawson, J.B.; Pinkerton, H.; Norton, G.E.; Pyle, D.M.; Browning, P.; Jackson, D.; Fallick, A.E. Petrology and geochemistry of Oldoinyo Lengai lavas extruded in November 1988: Magma source, ascent and crystallization. In *Carbonatite Volcanism: Oldoinyo Lengai and the Petrogenesis of Natrocarbonatites*; Bell, K., Keller, J., Eds.; Springer: Berlin, Germany, 1995; pp. 47–69.

6. Peterson, T.D.; Kjarsgaard, B. What are the parental magmas at Oldoinyo Lengai? In *Carbonatite Volcanism: Oldoinyo Lengai and the Petrogenesis of Natrocarbonatites*; Bell, K., Keller, J., Eds.; Springer: Berlin, Germany, 1995; pp. 148–162.

7. Keller, J.; Spettel, B. The trace element composition and petrogenesis of natrocarbonatites. In *Carbonatite Volcanism: Oldoinyo Lengai and the Petrogenesis of Natrocarbonatites*; Bell, K., Keller, J., Eds.; Springer: Berlin, Germany, 1995; pp. 70–86.

8. Bell, K.; Blenkinsop, J.; Cole, T.J.S.; Menagh, D.P. Evidence from Sr isotopes for long-lived heterogeneities in the upper mantle. *Nature* **1982**, *298*, 251–253.

9. Rukhlov, A.S.; Bell, K. Geochronology of carbonatites from the Canadian and Baltic Shields, and the Canadian Cordillera: Clues to mantle evolution. *Mineral. Petrol.* **2010**, *98*, 11–54.

10. Gold, D.P.; Eby, G.N.; Bell, K.; Vallée, M. Carbonatites, diatremes and ultra-alkaline rocks in the Oka area, Quebec. In *Geological Association of Canada Guidebook*; Geological Association of Canada: St. John's, NL, Canada, 1986.

11. Shafiqullah, M.; Tupper, W.; Cole, T. K-Ar age of the carbonatite complex, Oka, Quebec. *Can. Mineral.* **1970**, *10*, 541–552.

12. Wen, J.; Bell, K.; Blenkinsop, J. Nd and Sr isotope systematics of the Oka complex, Québec, and their bearing on the evolution of the sub-continental upper mantle. *Contrib. Mineral. Petrol.* **1987**, *97*, 433–437.

13. Cox, R.A.; Wilton, D.H.C. U-Pb dating of perovskite by LA-ICP-MS: An example from the Oka carbonatite, Quebec, Canada. *Chem. Geol.* **2006**, *235*, 21–32.

14. Chen, W.; Simonetti, A. *In-situ* determination of major and trace elements in calcite and apatite, and U-Pb ages of apatite from the Oka carbonatite complex: Insights into a complex crystallization history. *Chem. Geol.* **2013**, *353*, 151–172.

15. Chen, W.; Simonetti, A.; Burns, P.C. A combined geochemical and geochronological investigation of niocalite from the Oka carbonatite complex, Canada. *Can. Mineral.* **2013**, *51*, 785–800.

16. Eby, G. Geochronology of the Monteregian Hills alkaline igneous province, Quebec. *Geology* **1984**, *12*, 468–470.

17. Foland, K.A.; Gilbbert, L.A.; Sebring, C.A.; Chen, J.-F. ^{40}Ar/^{39}Ar ages for plutons of the Monteregian Hills, Quebec: Evidence for a single episode of Cretaceous magmatism. *Geol. Soc. Am. Bull.* **1986**, *97*, 966–974.

18. Mitchell, R.H.; Chakhmouradian, A.R. Instability of peroskite in a CO_2-rich environment: Examples from carbonatite and kimberlite. *Can. Mineral.* **1998**, *36*, 939–951.

19. Tappe, S.; Simonetti, A. Combined U-Pb geochronology and Sr-Nd isotope analysis of the Ice River perovskite standard, with implications for kimberlite and alkaline rock petrogenesis. *Chem. Geol.* **2012**, *304–305*, 10–17.

20. Simonetti, A.; Heaman, L.M.; Chacko, T. Use of discrete-dynode secondary electron multipliers with Faradays—A "reduced volume" approach for *in-situ* U-Pb dating of accessory minerals within petrographic thin section by LA-MC-ICP-MS. *Mineral. Assoc. Can. Short Course Ser.* **2008**, *40*, 241–264.

21. Wu, F.; Yang, Y.; Mitchell, R.H.; Li, Q.; Yang, J.; Zhang, Y. *In situ* U-Pb age determination and Nd isotopic analysis of perovkites from kimberlites in southern Africa and Somerset Island, Canada. *Lithos* **2010**, *115*, 205–222.

22. Zhang, D.; Zhang, Z.; Santosh, M.; Cheng, Z.; Huang, H.; Kang, J. Perovskite and baddeleyite from kimberlitic intrusions in the Tarim large igneous province signal the onset of an end-Carboniferous mantle plume. *Earth Planet. Sci. Lett.* **2013**, *361*, 238–248.

23. Koster van Groos, A.F.; Wyllie, P.J. Liquid immiscibility in the join $CaAl_2Si_2O_8$-$NaAlSi_3O_8$-Na_2CO_3-H_2O. *Am. J. Sci.* **1973**, *273*, 465–487.

24. Kjarsgaard, B.A.; Hamilton, D.L. Liquid immiscibility and the origin of alkali-poor carbonatites. *Mineral. Mag.* **1988**, *52*, 43–55.

25. Halama, R.; Vennemann, T.; Siebel, W.; Markl, G. The Grønnedal-Ika carbonatite-syenite complex, South Greenland: Carbonatite formation by liquid immiscibility. *J. Petrol.* **2005**, *46*, 191–217.

26. Brooker, R.A. The effect of CO_2 saturation on immiscibility between silicate and carbonate liquids: An experimental study. *J. Petrol.* **1998**, *39*, 1905–1915.

27. Lee, W.; Wyllie, P.J. Experimental data bearing on liquid immiscibility, crystal fractionation, and the origin of calciocarbonatite and natrocarbonatites. *Int. Geol. Rev.* **1994**, *36*, 797–819.

28. Korobeinikov, A.N.; Mitrofanov, F.P.; Gehör, S.; Laajoki, K.; Pavlov, V.P.; Mamontov, V.P. Geology and copper sulphide mineralization of the Salmagorskii ring igneous province, Kola Peninsula, NW Russia. *J. Petrol.* **1998**, *39,* 2033–2041.

29. Veksler, I.V.; Nielsen, T.F.D.; Sokolov, S.V. Mineralogy of crystallized melt inclusions from Gardiner and Kovdor ultramafic alkaline complexes: Implications for carbonatite genesis. *J. Petrol.* **1998**, *39*, 2015–2031.

30. Harmer, R.E.; Gittins, J. The Case for primary, mantle-derived carbonatite magma. *J. Petrol.* **1998**, *39*, 1895–1903.

31. Dalton, J.A.; Presnall, D.C. The continuum of primary carbonatitic-kimberlitic melt compositions in equilibrium with lherzolite: Data from the system CaO-MgO-Al_2O_3-SiO_2-CO_2 at 6 GPa. *J. Petrol.* **1998**, *39*, 1953–1964.

32. Bell, K.; Kjarsgaard, B.; Simonetti, A. Carbonatites-into the twenty-first century. *J. Petrol.* **1998**, *39*, 1839–1845.

33. Roulleau, E.; Pinti, D.L.; Stevenson, R.K.; Takahata, N.; Sano, Y.; Pitre, F. N, Ar and Pb isotopic co-variations in magmatic minerals: Discriminating fractionation processes from magmatic sources in Monteregian Hills, Québec, Canada. *Chem. Geol.* **2012**, *326–327*, 123–131.

34. Eby, G. Monteregian Hills I. Petrology, major and trace element geochemistry, and strontium isotopic chemistry of the western intrusions: Mounts Royal, St. Bruno, and Johnson. *J. Petrol.* **1984**, *25*, 421–452.

35. Pearce, N.J.G.; Perkins, W.T.; Westgate, J.A.; Gorton, M.P.; Jackson, S.E.; Neal, C.R.; Chenery, S.P. A compilation of new and published major and trace element data for NIST SRM 610 and NIST SRM 612 glass reference materials. *Geostand. Newsl.* **1997**, *21*, 115–144.

36. Van Acherbergh, E.; Ryan, C.G.; Jackson, S.E.; Griffin, W. Data reduction software for LA-ICP-MS. In *Laser Ablation-ICPMS in the Earth Science*; Sylvester, P., Ed.; Mineralogical Association of Canada: Quebec, QC, Canada, 2001; Volume 29, pp. 239–243.

37. Simonetti, A.; Neal, C.R. *In-situ* chemical, U-Pb dating, and Hf isotope investigation of megacrystic zircons, Malaita (Solomon Islands): Evidence for multi-stage alkaline magmatic activity beneath the Ontong Java Plateau. *Earth Planet. Sci. Lett.* **2010**, *295*, 251–261.

38. Thomson, S.N.; Gehrels, G.E.; Cecil, R.; Ruiz, J. Exploring routine laser ablation multicollector ICP-MS U-Pb dating of apatite. In Proceedings of the American Geophysical Union (AGU) Fall Meeting, San Francisco, CA, USA, 14–18 December 2009.

39. Storey, C.D.; Jeffries, T.E.; Smith, M. Common lead-corrected laser ablation ICP-MS U-Pb systematics and geochronology of titanite. *Chem. Geol.* **2006**, *227*, 37–52.

40. Simonetti, A.; Heaman, L.M.; Chacko, T.; Banerjee, N. *In-situ* petrographic thin section U-Pb dating of zircon, monazite, and titanite using laser ablation-MC-ICP-MS. *Int. J. Mass Spectrom.* **2006**, *253*, 87–97.

41. Banerjee, N.R.; Simonetti, A.; Furnes, H.; Muehlenbachs, K.; Staudigel, H.; Heaman, L.; van Kranendonk, M.J. Direct dating of Archean microbial ichnofossils. *Geology* **2007**, *35*, 487–490.

42. Grünenfelder, M.H.; Tilton, G.R.; Bell, K.; Blenkinsop, J. Lead and strontium isotope relationships in the Oka carbonatite complex, Quebec. *Geochim. Cosmochim. Acta* **1986**, *50*, 461–468.

43. Chew, D.M.; Sylvester, P.J.; Tubrett, M.N. U-Pb and Th-Pb dating of apatite by LA-ICPMS. *Chem. Geol.* **2011**, *280*, 200–216.

44. Horstwood, M.S.A.; Foster, G.L.; Parrish, R.R.; Noble, S.R.; Nowell, G.M. Common-Pb corrected *in situ* U-Pb accessory mineral geochronology by LA-MC-ICP-MS. *J. Anal. At. Spectrom.* **2003**, *18*, 837–846.

45. Simonetti, A.; Heaman, L. U-Pb zircon dating by laser ablation-MC-ICP-MS using a new multiple ion counting Faraday collector array. *J. Anal. At. Spectrom.* **2005**, *20*, 677–686.

46. Ludwig, K.R. *User's Manual for Isoplot 3.00: A Geochronological Toolkit for Microsoft Excel*; Berkeley Geochronology Center: Berkeley, CA, USA, 2003.

47. Paton, C.; Woodhead, J.D.; Hergt, J.M.; Phillips, D.; Shee, S. Strontium isotope analysis of groundmass perovskite via LA-MC-ICP-MS. *Geostand. Geoanal. Res.* **2007**, *31*, 321–330.

48. Ramos, F.C.; Wolf, J.A.; Tollstrup, D.L. Measuring $^{87}Sr/^{86}Sr$ variations in minerals and groundmass from basalts using LA-MC-ICP-MS. *Chem. Geol.* **2004**, *211*, 135–158.

49. Bizzarro, M.; Simonetti, A.; Stevenson, R.K.; Kurszlaukis, S. *In situ* $^{87}Sr/^{86}Sr$ investigation of igneous apatites and carbonates using laser ablation MC-ICP-MS. *Geochim. Cosmochim. Acta* **2003**, *67*, 289–302.

50. Wasserburg, G.J.; Jacobsen, S.B.; DePaolo, D.J.; McCulloch, M.T.; Wen, T. Precise determination of Sm/Nd ratios, Sm and Nd isotopic abundances in standard solutions. *Geochim. Cosmochim. Acta* **1981**, *45*, 2311–2323.

51. Yang, Y.H.; Zhang, H.F.; Xie, L.W.; Wu, F. Accurate measurement of neodymium isotopic composition using Neptune multiple collector inductively coupled plasma mass spectrometry. *Chin. J. Anal. Chem.* **2007**, *35*, 71–74.

52. McFarlane, C.; McCulloch, M. Sm-Nd and Sr isotope systematics in LREE-rich accessory minerals using LA-MC-ICP-MS. *V.M. Goldschmidt Laser Ablation Short Course Vol.* **2008**, *40*, 117–134.

53. Chakhmouradian, A.R.; Mitchell, R.H. Occurrence, alteration patterns and compositional variation of perovskite in kimberlites. *Can. Mineral.* **2000**, *38*, 975–994.

54. Chakhmouradian, A.R.; Mitchell, R.H. Three compositional varieties of perovskite from kimberlites of the Lac de Gras field (Northwest Territories, Canada). *Mineral. Mag.* **2001**, *65*, 133–148.

55. McDonough, X.F.; Sun, S. The composition of the Earth. *Chem. Geol.* **1995**, *120*, 223–253.

56. Wendt, I.; Carl, C. The statistical distribution of the mean squared weighted deviation. *Chem. Geol.* **1991**, *35*, 696–698.

57. Vermeesch, P. On the visualisation of detrital age distributions. *Chem. Geol.* **2012**, *312–313*, 190–194.

58. Bell, K.; Blenkinsop, J. Nd and Sr isotopic compositions of East African carbonatites: Implications for mantle heterogeneity. *Geology* **1987**, *15*, 99–102.

59. Heaman, L.M.; Kjarsgaard, B.A. Timing of eastern North American kimberlite magmatism: Continental extension of the Great Meteor hotspot track? *Earth Planet. Sci. Lett.* **2000**, *178*, 253–268.

60. Secher, K.; Heaman, L.M.; Nielsen, T.F.D.; Jensen, S.M.; Schjøth, F.; Creaser, R.A. Timing of kimberlite, carbonatite, and ultramafic lamprophyre emplacement in the alkaline province located 64°–67° N in southern West Greenland. *Lithos* **2009**, *112*, 400–406.

61. Tappe, S. Genesis of Ultramafic Lamprophyres and Carbonatites at Aillik Bay, Labrador: A Consequence of Incipient Lithospheric Thinning beneath the North Atlantic Craton. *J. Petrol.* **2006**, *47*, 1261–1315.

62. Tappe, S.; Pearson, D.G.; Nowell, G.; Nielsen, T.; Milstead, P.; Muehlenbachs, K. A fresh isotopic look at Greenland kimberlites: Cratonic mantle lithosphere imprint on deep source signal. *Earth Planet. Sci. Lett.* **2011**, *305*, 235–248.

63. Tappe, S.; Steenfelt, A.; Heaman, L.M.; Simonetti, A. The newly discovered Jurassic Tikiusaaq carbonatite-aillikite occurrence, West Greenland, and some remarks on carbonatite–kimberlite relationships. *Lithos* **2009**, *112*, 385–399.

64. Smith, C. Pb, Sr and Nd isotope evidence for sources of southern African Cretaceous kimberlites. *Nature* **1983**, *304*, 51–54.

65. Zartman, R.E.; Richardson, S.H. Evidence from kimberlitic zircon for a decreasing mantle Th/U since the Ardean. *Chem. Geol.* **2005**, *220*, 263–283.

66. Zurevinski, S.E.; Heaman, L.M.; Creaser, R.A. The origin of Triassic/Jurassic kimberlite magmatism, Canada: Two mantle sources revealed from the Sr-Nd isotopic composition of groundmass perovskite. *Geochem. Geophys. Geosyst.* **2011**, *12*, doi:10.1029/2011GC003659.

67. Zurevinski, S.E.; Heaman, L.M.; Creaser, R.A.; Strand, P. The Churchill kimberlite field, NU, Canada: Petrography, mineral chemistry and geochronology. *Can. J. Earth Sci.* **2008**, *45*, 1039–1059.

68. Zurevinski, S.E.; Mitchell, R.H. Extreme compositional variation of pyrochlore-group minerals at the Oka Carbonatite complex, Quebec: Evidence of magma mixing? *Can. Mineral.* **2004**, *42*, 1159–1168.

69. McHone, J.G. Constraints on the mantle plume model for Mesozoic alkaline intrusions in northeastern North America. *Can. Mineral.* **1996**, *34*, 325–334.

70. Faure, S.; Tremblay, A.; Angelier, J. State of intraplate stress and tectonism of northeastern America since Cretaceous times, with particular emphasis on the New-England-Quebec igneous province. *Tectonophysics* **1986**, *255*, 111–134.

71. Crough, S. Mesozoic hotspot epeirogeny in eastern North America. *Geology* **1981**, *9*, 2–6.

72. Duncan, R.A. Age progressive volcanism in the New England seamounts and the opening of the central Atlantic Ocean. *J. Geophys. Res.* **1984**, *89*, 9980–9990.

73. Sleep, N.H. Monteregian hotspot track: A long-lived mantle plume. *J. Geophys. Res.* **1990**, *95*, 21983–21990.

74. Burke, K.; Khan, S.D.; Mart, R.W. Grenville province and Monteregian carbonatite and nepheline syenite distribution related to rifting, collision, and plume passage. *Geology* **2008**, *36*, 983–986.

75. Simonetti, A.; Bell, K. Nd, Pb and Sr isotopic data from the Napak carbonatite-nephelinite centre, eastern Uganda: An example of open-system crystal fractionation. *Contrib. Mineral. Petrol.* **1994**, *115*, 356–366.

76. Hart, S.R.; Gerlach, D.C.; White, W.M. A possible new Sr-Nd-Pb mantle array and consequences for mantle mixing. *Geochim. Cosmochim. Acta* **1986**, *50*, 1551–1557.

77. Bell, K.; Tilton, G. Probing the mantle: The story from carbonatites. *Eos Trans. Am. Geophys. Union* **2002**, *83*, 273–277.

78. Bell, K.; Simonetti, A. Carbonatite magmatism and plume activity: Implications from the Nd, Pb and Sr isotope systematics of Oldoinyo Lengai. *J. Petrol.* **1996**, *37*, 1321–1329.

79. Simonetti, A.; Bell, K.; Viladkar, S.G. Isotopic data from the Amba Dongar carbonatite complex, West-central India: Evidence for an enriched mantle source. *Chem. Geol.* **1995**, *122*, 185–198.

80. Simonetti, A.; Goldstein, S.L.; Schmidberger, S.S.; Viladkar, S.G. Geochemical and Nd, Pb, and Sr isotope data of Deccan alkaline complexes—Inferences on mantle sources and plume-lithosphere interaction. *J. Petrol.* **1998**, *39*, 1847–1864.

81. Tilton, G.R.; Bell, K. Sr-Nd-Pb isotope relationships in late Archean carbonatites and alkaline complexes: Applications to the geochemical evolution of Archean mantle. *Geochim. Cosmochim. Acta* **1994**, *58*, 3145–3154.

82. Bell, K.; Simonetti, A. Source of parental melts to carbonatites-critical isotopic constraints. *Mineral. Petrol.* **2010**, *98*, 77–89.

83. Hoernle, K.; Tilton, G.; le Bas, M.J.; Duggen, S.; Garbe-Schönberg, D. Geochemistry of oceanic carbonatites compared with continental carbonatites: Mantle recycling of oceanic crustal carbonate. *Contrib. Mineral. Petrol.* **2002**, *142*, 520–542.

84. Rondenay, S.; Bostock, M.G.; Hearn, T.M.; White, D.J.; Ellis, R.M. Lithospheric assembly and modification of the SE Canadian Shield: Abitibi-Grenville teleseismic experiment. *J. Geophys. Res.* **2000**, *105*, 13735–13754.

85. Aktas, K.; Eaton, D.W. Upper-mantle velocity structure of the lower Great Lakes region. *Tectonophysics* **2006**, *420*, 267–281.

86. Eby, G.N. Age relations, chemistry, and petrogenesis of mafic alkaline dykes from the Monteregian Hills and younger White Mountain igneous provinces. *Can. J. Earth Sci.* **1985**, *22*, 1103–1111.

87. Samson, I.M.; Liu, W.; Williams-Jones, A.E. The nature of orthomagmatic hydrothermal fluids in the Oka carbonatite, Quebec, Canada: Evidence from fluid inclusions. *Geochim. Cosmochim. Acta* **1995**, *59*, 1963–1977.